



NTNU – Trondheim
Norwegian University of
Science and Technology

Direct numerical simulation of turbulent flow in a channel with transverse ribs

Tor Holan Marstein

Master of Science in Mechanical Engineering

Submission date: February 2015

Supervisor: Helge Ingolf Andersson, EPT

Co-supervisor: Lihao Zhao, EPT

Norwegian University of Science and Technology
Department of Energy and Process Engineering

EPT-M-2014-68

MASTEROPPGAVE

for

Student Tor Holan Marstein

Høsten 2014

Numerisk simulering av turbulent strømning i kanal med tversgående ruhet*Numerical simulation of turbulent flow in a channel with transverse ribs***Bakgrunn og målsetting**

Tversgående ribber er ofte benyttet for å studere effekten av veggruhet på turbulent strømning. Likeledes benyttes tversgående ribber for å øke varmegjennomgangen i gassturbiner. Størrelsen på og avstanden mellom ribbene er da viktige parametre. Målsettingen med oppgaven er å ta i bruk et 'in-house' simuleringsverktøy utviklet for direkte numerisk simulering (DNS) av enkel kanalstrømning med glatte vegger. Denne FORTRAN-koden benytter fast-Fourier transformeringer (FFT) i både bredde- og lengderetningen. Det vil derfor være en utfordring å undersøke hvordan koden oppfører seg når tversgående ribber implementeres langs kanalveggene. Et åpent spørsmål blir derfor hvor høye ribbene kan være før det går ut over nøyaktigheten til simuleringene.

Oppgaven bearbeides ut fra følgende punkter

- 1 Begrenset litteraturstudium om turbulent strømning over ru overflater
- 2 Direkte numerisk simulering av turbulent strømning i plan kanal
- 3 Simulering av turbulent strømning i kanal med tversgående ribber
- 4 Sammenligning av resultatene fra pkt 2 og 3 med resultater i litteraturen
- 5 Parameterstudie (hvis tiden tillater det)

Senest 14 dager etter utlevering av oppgaven skal kandidaten levere/sende instituttet en detaljert fremdrift- og eventuelt forsøksplan for oppgaven til evaluering og eventuelt diskusjon med faglig ansvarlig/veiledere. Detaljer ved eventuell utførelse av dataprogrammer skal avtales nærmere i samråd med faglig ansvarlig.

Besvarelsen redigeres mest mulig som en forskningsrapport med et sammendrag både på norsk og engelsk, konklusjon, litteraturliste, innholdsfortegnelse etc. Ved utarbeidelsen av teksten skal kandidaten legge vekt på å gjøre teksten oversiktlig og velkrevet. Med henblikk på lesning av besvarelsen er det viktig at de nødvendige henvisninger for korresponderende steder i tekst, tabeller og figurer anføres på begge steder. Ved bedømmelsen legges det stor vekt på at resultatene er grundig bearbeidet, at de oppstilles tabellarisk og/eller grafisk på en oversiktlig måte, og at de er diskutert utførlig.

Alle benyttede kilder, også muntlige opplysninger, skal oppgis på fullstendig måte. For tidsskrifter og bøker oppgis forfatter, tittel, årgang, sidetall og eventuelt figurnummer.

Det forutsettes at kandidaten tar initiativ til og holder nødvendig kontakt med faglærer og veileder(e). Kandidaten skal rette seg etter de reglementer og retningslinjer som gjelder ved alle (andre) fagmiljøer som kandidaten har kontakt med gjennom sin utførelse av oppgaven, samt etter eventuelle pålegg fra Institutt for energi- og prosesssteknikk.

Risikovurdering av kandidatens arbeid skal gjennomføres i henhold til instituttets prosedyrer. Risikovurderingen skal dokumenteres og inngå som del av besvarelsen. Hendelser relatert til kandidatens arbeid med uheldig innvirkning på helse, miljø eller sikkerhet, skal dokumenteres og inngå som en del av besvarelsen. Hvis dokumentasjonen på risikovurderingen utgjør veldig mange sider, leveres den fulle versjonen elektronisk til veileder og et utdrag inkluderes i besvarelsen.

I henhold til "Utfyllende regler til studieforskriften for teknologistudiet/sivilingeniørstudiet" ved NTNU § 20, forbeholder instituttet seg retten til å benytte alle resultater og data til undervisnings- og forskningsformål, samt til fremtidige publikasjoner.

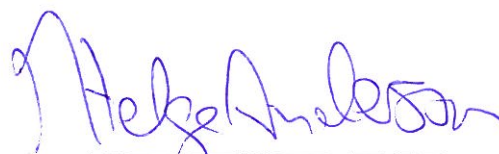
Besvarelsen leveres digitalt i DAIM. Et faglig sammendrag med oppgavens tittel, kandidatens navn, veileders navn, årstall, instituttnavn, og NTNUs logo og navn, leveres til instituttet som en separat pdf-fil. Etter avtale leveres besvarelse og evt. annet materiale til veileder i digitalt format.

- Arbeid i laboratorium (vannkraftlaboratoriet, strømningsmeknisk, varmeteknisk)
 Feltarbeid

NTNU, Institutt for energi- og prosesssteknikk, 24. september 2014



Olav Bolland
Instituttleder



Helge Andersson
Faglig ansvarlig/veileder

Medveileder: Dr Lihao Zhao

Abstract

Surface roughness is of great relevance in most engineering applications, as very few surfaces can be regarded as perfectly smooth. Investigation of the effects on the mean flow, as well as the near wall turbulence is therefore of interest.

In the present study, all scales of the turbulent motions are resolved using Direct Numerical Simulation (DNS). Transverse square ribs are introduced as a surface roughness model in a pressure driven channel flow at Reynolds number $Re_\tau = 395$ to establish a streamwise inhomogeneity. The principal aim of the study is to see whether a specific in-house pseudo-spectral DNS-code developed for plane channel flow performs, even though it is, in principle, not suited for this specific application.

The results from the rough channel simulation are compared to both a smooth and rough channel reference case. The results are found to be almost identical to that of the rough channel reference. For the mean velocity profile, the logarithmic shape is maintained, but the profile has a downwards shift due to the increased drag. Streamwise dependency for the mean velocity, as well as turbulence quantities, is found to be limited to the roughness sublayer, stretching out to $z^+ \approx 5r^+$, where r^+ is the non-dimensionalized height of the roughness elements, indicating that the flow is unaware of the surface conditions in the outer region. Compared to the smooth channel data, roughness effects are mainly found to affect the flow inside the roughness sublayer.

It is proven that the pseudo-spectral DNS-code works well with the relatively small roughness elements, and despite the fact that streamwise homogeneity is removed, the results suggests that the quasi-homogeneity of the velocity field is sufficient for the pseudo-spectral code to deliver accurate results. Further, when accounting for reduced domain size, the grid point resolution is 43% less than in the reference case of Ashrafian [4]. This is motivated by reduced computational cost, but also serves as a check on the spectral-method's superior accuracy and reduced demand for grid point resolution. The results indicates that a relatively high level of accuracy is still delivered.

Sammendrag

Effekten av veggruhet er av høy relevans når det kommer til industrielle strømnings, siden de fleste flater ikke kan antas å være perfekt glatte. Å undersøke hvilke konsekvenser veggruhet får for den midlere strømmingen og turbulensen er derfor av interesse.

I oppgaven løses alle skalaer av den turbulente strømmingen opp ved hjelp av direkte numerisk simulering (DNS). Tversgående, kvadratiske ribber implementeres som en ruhetsmodell i en trykkdrevet kanalstrømning med Reynoldstall $Re_\tau = 395$ for å etablere inhomogen strømning i hovedstrømsretning. Hovedintensjonen er å undersøke om et "in-house" simuleringsverktøy utviklet for turbulent strømning i glatt kanal fungerer, selv om koden i prinsippet ikke er ment å fungere for slik strømning.

Resultatene fra kanalstrømmingen med veggruhet sammenlignes med to referanse-simuleringer, én for glatt kanal og én for ru kanal. Resultatene er nærmest identiske med de som er funnet for den reue kanalen. Den logaritmiske profilen til det midlele hastighetsprofilen opprettholdes, men får et vertikalt skift på grunn av høyere strømningsmotstand. Avhengighet i hovedstrømsretning er funnet å være begrenset til det vegg-nære ruhetssjiktet som strekker seg ut til $z^+ \approx 5r^+$ for både hastighetsprofilen og ulike turbulensvariabler. Her er r^+ den veggnormaliserte høyden til ruhetselementene. Dette indikerer at strømmingen er upåvirket av forholdene på veggen i det ytre området. Sammenlignet med strømning i glatt kanal, er effektene fra ruhet funnet å påvirke strømmingen hovedsaklig bare i dette ruhetssjiktet.

Det er altså vist at den pseudo-spektrale DNS-koden virker med de forholdsvis små ruhetselementene som er undersøkt. Selv om strømmingen ikke lenger er homogen i hovedstrømsretning, indikerer resultatene at periodisiteten som oppstår i denne retningen er nok til at koden gir nøyaktige resultater. Tatt den reduserte domenestørrelsen i betraktning, er tettheten av gridpunkter redusert med 43% sammenliknet med det som er benyttet i Ashrafian [4]. Dette er motivert av redusert behov for datakraft og lagringskapasitet, men også som en sjekk på spektral-metodens høye nøyaktighet og begrensede krav til gridpunkt-tetthet. Resultatene indikerer at en relativt høy nøyaktighet fortsatt leveres.

Preface

This master thesis is written in the fall of 2014 at the Department of Energy and Process Engineering at the Norwegian University of Science and Technology.

The thesis is not a continuous work from the project thesis, thus there were many new concepts to get hold on. I would like to thank my supervisor, professor Helge I. Andersson, for the proposal and guidance of work. Also, I had the opportunity to follow his higher level course, EP8405 Turbulence, during the fall, to further increase my knowledge on turbulence and modelling of statistics.

Further, I appreciate the assistance of my co-supervisor, Dr. Lihao Zhao, who has provided excellent guidance throughout the work regarding the DNS-code, using the HPC-facilities at NTNU and post processing of results.

Tor Holan Marstein
Trondheim, 17.02.2015

Contents

Abstract	iii
Sammendrag	v
Preface	vii
Table of contents	ix
Nomenclature	xi
1 Introduction	1
1.1 Motivation	1
1.2 Outline	2
2 Turbulence	3
2.1 Turbulent flows	3
2.2 Governing equations for fluid motion	4
2.3 A statistical approach	6
2.4 Equations of turbulence	7
2.5 The energy cascade and range of scales	10
2.6 Isotropic and homogeneous turbulence	11
3 Channel flow with roughness	13
3.1 A historical overview	13
3.2 Flow regimes	14
3.3 Mean velocity profiles	15
3.4 Roughness classifications	17
3.5 The roughness sublayer and wall similarity	18
3.6 Numerical simulation	20
4 Numerical approach	23
4.1 Direct Numerical Simulation	23
4.2 Pressure-velocity coupling	24
4.3 Discretization	25
4.4 Simulation setup	30

5	Smooth channel results	37
5.1	Mean velocity profiles	38
5.2	Turbulence intensities	39
5.3	Reynolds shear stress	41
5.4	Vorticity	41
6	Rough channel results	45
6.1	Mean velocity profiles	47
6.2	Turbulence intensities	50
6.3	Reynolds stresses	54
6.4	Reynolds shear stress	57
6.5	Turbulence kinetic energy	57
6.6	Vorticity	59
7	Discussion	61
7.1	Statistics	61
7.2	Domain size	61
7.3	Grid resolution	62
7.4	Roughness elements	63
7.5	Inhomogeneity	64
7.6	Further work	64
8	Conclusion	67
	References	69

Nomenclature

Roman symbols

d_{ij}	Diffusion terms in transport equation for RST	$(\text{m}^2 \text{s}^{-3})$
d_k	Diffusion terms in transport equation for TKE	$(\text{m}^2 \text{s}^{-3})$
f_i	Body forces in x_i direction	(kg m s^{-2})
g	Gravitational acceleration	(m s^{-2})
h	Channel height	(m)
k	Turbulence kinetic energy	$(\text{m}^2 \text{s}^{-2})$
k	Wavenumber	(m^{-1})
k_s	Equivalent sand-grain roughness	(m)
L	Characteristic length of bounding geometry	(m)
l_0	Integral length scale	(m)
Ma	Mach number	(dimensionless)
p	Pressure	$(\text{kg m}^{-1} \text{s}^{-2})$
P_{ij}	Production rate tensor of Reynolds stress	$(\text{m}^2 \text{s}^{-3})$
P_k	Production rate of TKE	$(\text{m}^2 \text{s}^{-3})$
r	Roughness height	(m)
Re_b	Reynolds number based on bulk velocity and channel half-height	(dimensionless)
Re_0	Reynolds number based on integral scale	(dimensionless)
Re_t	Reynolds number based on turbulence length scale	(dimensionless)
Re_τ	Reynolds number based on shear velocity and channel half-height	(dimensionless)
$Re_{\tau,h}$	Reynolds number based on shear velocity and channel height	(dimensionless)
S_{ij}	Strain-rate tensor	(s^{-1})

T	Temperature	(K)
t	Time	(s)
U	Characteristic flow velocity scale	(m s ⁻¹)
u_0	Integral velocity scale	(m s ⁻¹)
U_b	Bulk velocity	(m s ⁻¹)
u_{CL}	Channel centerline velocity	(m s ⁻¹)
u_η	Kolmogorov velocity scale	(m s ⁻¹)
\hat{u}_k	Discrete Fourier coefficients of the function u	()
u_τ	Friction velocity / wall shear velocity	(m s ⁻¹)
u	Streamwise velocity component, u_1	(m s ⁻¹)
v	Spanwise velocity component, u_2	(m s ⁻¹)
w	Wall-normal velocity component, u_3	(m s ⁻¹)
x	Streamwise coordinate, x_1	(m)
y	Spanwise coordinate, x_2	(m)
z	Wall-normal coordinate, x_3	(m)

Greek Symbols

δ	Channel half-height	(m)
δ_{ij}	Kronecker delta function	()
ε	Rate of dissipation	(m ² s ⁻³)
ε_{ij}	Dissipation tensor	(m ² s ⁻³)
η	Kolmogorov length scale	(m)
κ	von Kármán constant	()
λ	Height-to-pitch ratio	()
μ	Dynamic viscosity	(kg m ⁻¹ s ⁻¹)
μ_T	Dynamic turbulence viscosity	(kg m ⁻¹ s ⁻¹)
ν	Kinematic viscosity	(m ² s ⁻¹)
ν_T	Kinematic turbulence viscosity	(m ² s ⁻¹)
ϕ	Scalar transport-variable	()
Φ_{ij}	Pressure-strain tensor	(m ² s ⁻³)
ρ	Density	(kg m ⁻³)
τ_0	Integral time scale	(s)

τ_η	Kolmogorov time scale	(s)
τ_{ij}	Stress tensor	(kg m ⁻¹ s ⁻²)
τ_w	Wall shear stress	(kg m ⁻¹ s ⁻²)

Sub- and superscripts

- $\bar{\bullet}$ Averaged quantity; alternatively $\langle \bullet \rangle$
- \bullet' Fluctuating quantity
- \bullet^* Non-dimensionalized quantity
- \bullet^+ Wall-normalized quantity

Abbreviations

AB2	Adams-Bashforth (2nd order accurate)
CFD	Computational Fluid Dynamics
CFL	Courant-Friedrichs-Lewy
DES	Detached Eddy Simulation
DNS	Direct Numerical Simulation
FDM	Finite Difference Method
FEM	Finite Element Method
FFT	Fast Fourier Transform
FORTTRAN	FORmula TRANslation
FVM	Finite Volume Method
HPC	High Performance Computing
LES	Large Eddy Simulation
RANS	Reynolds Averaged Navier-Stokes equations
RSM	Reynolds Stress Modelling
RST	Reynolds Stress Tensor
SEM	Spectral Element Method
SMC	Second Moment Closures
TKE	Turbulence Kinetic Energy

List of Figures

2.1	The effect of averaging the flow field	7
2.2	The energy cascade	10
3.1	Moody chart.	15
3.2	Mean velocity profile shift.	17
3.3	Classification of roughness.	18
4.1	Aliasing error	30
4.2	Roughness parameters	31
4.3	Flow domain	32
4.4	Grid discretization in z -direction	33
4.5	Roughness element modelling	34
5.1	Mean velocity, global coordinates	38
5.2	Mean velocity, wall coordinates	39
5.3	R.m.s. of velocity fluctuations, global coordinates	40
5.4	R.m.s. of velocity fluctuations, wall coordinates	40
5.5	Shear stress distribution, wall coordinates	41
5.6	R.m.s. of vorticity fluctuations, global coordinates	42
5.7	R.m.s. of vorticity fluctuations, wall coordinates	42
6.1	Instantaneous and averaged contour plot	46
6.2	Evolution of the bulk velocity in time	46
6.3	Mean streamwise velocity, global coordinates	47
6.4	Mean streamwise velocity, global coordinates	48
6.5	Mean spanwise and wall-normal velocities	49
6.6	Streamlines between roughness crests	49
6.7	Turbulence intensity in global coordinates	50
6.8	R.m.s. of velocity fluctuations, global coordinates	51
6.9	R.m.s. of velocity fluctuations, wall coordinates	53
6.10	R.m.s. of velocity fluctuations from Ashrafian & Andersson [5].	53
6.11	Reynolds streamwise normal stress, global coordinates	54
6.12	Reynolds spanwise normal stress, global coordinates	55
6.13	Reynolds wall-normal normal stress, global coordinates	56
6.14	Reynolds shear stress, global coordinates	56
6.15	Shear stress distribution, wall coordinates	57
6.16	Instantaneous and averaged contour plot of the TKE	58
6.17	Turbulence kinetic energy, wall coordinates	59

6.18 R.m.s. of vorticity fluctuations, wall coordinates	60
---	----

List of Tables

4.1	Domain details for the smooth and rough case	32
4.2	Mesh resolution details for the smooth and rough case	33
5.1	Domain and mesh resolution for the smooth channel	37
6.1	Domain and mesh resolution for the rough channel	45

1 Introduction

As very few surfaces in real life applications can be regarded as perfectly smooth, roughness is of great importance in engineering. The introduction of surface roughness has a significant impact on the near wall flow structure and overall characteristics of the flow. By generating irregular turbulent motion in the very near-wall region, and extending the surface into the flow, heat transfer rate is enhanced. At the same time however, flow resistance, that is the drag force exerted by the walls, increases. This is of special interest regarding pressure loss in pipes and long pipelines. Small devices, that in effect produces a rough surface, can also be used to suppress or promote transition from laminar to turbulent flow. Further, the effect of rough walls is highly relevant in high Reynolds number applications, such as flows over ship hulls and aircraft fuselage, as the roughness becomes large compared to the near-wall viscous length scales.

In an engineering computation perspective, however, the details of the roughness cannot be represented without extreme computational cost, and models are used in most engineering problems where roughness is believed to be of significance. Thus, increased understanding of turbulence modifications for use with statistical closure models is highly needed.

Direct Numerical Simulation is the most computer demanding approach used to deal with the complexity of turbulence, but on the other hand, it allows for very detailed and accurate investigation of small scale flow behaviour. It also allows for specific types of roughness to be studied efficiently. In the present case, spanwise rectangular ribs is investigated. Such rod roughness provides a considerable rough boundary for the flow, and many studies on this specific type of roughness has been conducted. Despite a great amount of research, there are still controversy in how, and to what extent events in the very near-wall layer affects the turbulence in the outer flow.

1.1 Motivation

As mentioned, computer demanding direct simulation is used to resolve all scales of the turbulent motions. Naturally, this demands a great deal of available computational power, but also efficient numerical procedures to handle the large number

of required computational operations. Dealing with partial differential equations, spectral methods offers superior accuracy and performance, as the variables are replaced with Fourier-series representations, and by use of computer efficient Fast Fourier transform- algorithms (FFT), calculation of exact derivatives is performed in Fourier space, where differentiation is a straight forward multiplication operation. Thus, many DNS-codes for simple flows use spectral numerics.

In spectral methods, the basis functions, the complex Fourier series, has a global support, which means they are non-zero over the whole domain. This requires the variables being represented to be periodic functions, which effectively implies that the flow must be homogeneous in the specified direction. Further, such methods implies restrictions on the boundary conditions, which must be periodic, as well as the grid spacing, which must be uniform. In addition, the solution must be smooth, as the method is not capable of capturing discontinuities such as shock-waves. Thus, spectral methods, at least in the beginning, were most suited for simulation of very simple homogeneous and isotropic turbulence. Later, advances has been made in expanding its applicability to cover flows with multiple inhomogeneous directions. One class of such methods is Spectral Element Methods (SEM), where the basis functions are restricted to only having a local support on a small part of the domain, similar to that in Finite Element Methods (FEM). This allows for both complex geometries to be represented and the use of more flexible numerical grids.

The aim of the present study is, however, to introduce rod roughness in a DNS-code developed for plane channel flow. The code uses a spectral-method in homogeneous directions, spanwise and streamwise direction, and finite differences in the inhomogeneous wall-normal direction. The primary motivation is to see whether the spectral method still performs, despite the fact that streamwise homogeneity now is removed due to the presence of obstacles. The results, and how the flow is affected by the roughness will be compared to available data from the previous work of Ashrafian [4].

1.2 Outline

The basic outline of the thesis is that chapter 2, 3 and partly 4 gives a theoretical foundation, while chapter 5, 6 and 7 are concerned with the simulations.

In chapter 2, governing equations for fluid motion is presented. Fundamental theory and mechanisms of turbulence is discussed to gain knowledge on the treatment of such flows. Strictly speaking, there is perhaps somewhat more focus on turbulence fundamentals included here, than what is actually necessary. Further, chapter 3 gives an introduction to wall-roughness, and how this affects the mean flow field, as well as the turbulence. Also, a brief overview on findings from literature on the topic is included. As a proceeding from chapter 2, numerical aspects is discussed in chapter 4. Solution strategies and computer implementation of the equations, together with the numerical setup of the simulation is given. In chapter 5 and 6, the results from the smooth- and rough-wall simulation are presented, complemented by a discussion in chapter 7.

2 Turbulence

For a start, a short introduction to some fundamental theory on fluid mechanics and turbulence are given. This includes the governing equations for fluid motion, mathematical tools used to describe a turbulent flow field and equations giving a more detailed insight into important mechanisms of turbulence.

From a computational point of view, numerous approaches to handle the complexity of turbulent flows exists. Most engineering computations are based on averaged equations (RANS), which requires a high degree of modelling. As computational resources has become more available, simulation techniques that partially resolves the turbulent eddies are also used to a wider extent. This is called Large Eddy Simulation (LES). In recent years, advances has also been made in formulations of hybrid approaches such as hybrid LES-RANS (e.g. DES). DNS, however, fully resolves the turbulent motion, and is maybe the most straightforward way to solve the Navier-Stokes equations numerically. However, due to computational cost, this is in great contrast to engineering computations, and it should be emphasized that DNS as a numerical tool is a pure research tool for solving simple flows, and not "*a brute force solution to the Navier-Stokes equations for engineering problems*" [40, p.539].

To obtain a compact and efficient writing of equations, Cartesian tensor notation is used. For a three-dimensional coordinate system this yields $i, j, k = 1, 2, 3$, such that $u_1 = u$, $u_2 = v$, $u_3 = w$ for the velocities, and $x_1 = x$, $x_2 = y$, $x_3 = z$ for the spatial coordinates.

2.1 Turbulent flows

Most flows encountered in engineering applications and more generally in every-day life are turbulent. Qualitatively, this is easily recognized by a highly irregular nature, seemingly random and chaotic motions and vortices, all of which are spanning over a large range of temporal and spatial scales. In this unpredictable flow state, viscous effects are no longer able to damp instabilities and small perturbations. An important dimensionless parameter, the Reynolds number, Re , can be used to identify flow regime. Basically, this is just a measure of inertia to viscous forces, and as a consequence, turbulent flows are characterized by high Reynolds numbers.

The physics of turbulence is not yet fully understood, thus a formal definition may not exist. However, there are some properties that are always present when a flow is classified as turbulent.

Three-dimensional and time dependent

The velocity fluctuations will always be in all spatial directions, varying in time.

Range of scales

The flow contains a whole spectra of scales in both time and space. The largest scales, the integral scales, is of the order of the limiting geometry in space, and the smallest, the Kolmogorov scales, is almost at a microscopic level.

Diffusive

Transport and spreading of momentum and scalars such as heat and mass will always be higher in turbulent flow due to fluctuations and irregularity.

Dissipative

From the smallest scales, where viscous effects are significant, energy is dissipated into heat. This is why turbulent flows have increased energy losses.

2.2 Governing equations for fluid motion

Three fundamental physical principles on which all fluid dynamics is based upon is conservation of mass, balance of momentum, and conservation of energy, where the two latter are Newtons 2. law and the first law of thermodynamics. When these principles are applied to a bounded, three dimensional space in the continuous fluid, mathematical statements expressing the physics can be derived. Here, this space, the control volume, is chosen to be an infinitesimal fluid element fixed in space. Thus, the governing equations are written in differential and conservative form¹.

Continuity, equation (2.1), states that mass is conserved, while Newtons 2. law, equation (2.2), expresses a balance of momentum. In fluid dynamics, the latter is known as the Navier-Stokes equations.

$$\frac{\partial \rho}{\partial t} + \frac{\partial}{\partial x_i}(\rho u_i) = 0 \quad (2.1)$$

$$\frac{\partial}{\partial t}(\rho u_i) + \frac{\partial}{\partial x_j}(\rho u_i u_j) = \frac{\partial}{\partial x_j} \left(-p \delta_{ij} + 2\mu S_{ij} - \frac{2}{3}\mu \frac{\partial u_k}{\partial x_k} \delta_{ij} \right) + \rho f_i \quad (2.2)$$

The left side in equation (2.2) is simply the acceleration term, while the right side is a summation of all the forces acting on the fluid element. For a Newtonian fluid, the viscous shear stress is written as a linear function of the strain rate, as can be seen in the second term on the right side. The third term expresses dissipation linked

¹Similarly, equations on integral form can be derived from a control volume of finite size. This forms the basis for the Finite Volume Method (FVM) widely used in CFD. Both forms are equally valid.

to change of volume of the element. The constant $-\frac{2}{3}\mu$ is simply given by Stoke's hypothesis [49], while δ_{ij} is the Kronecker delta function. f_i is the body forces acting on the entire mass of the fluid element and S_{ij} is the strain rate tensor, which is symmetric for isotropic fluids [49].

$$S_{ij} = \frac{1}{2} \left(\frac{\partial u_i}{\partial x_j} + \frac{\partial u_j}{\partial x_i} \right) \quad (2.3)$$

Until now, conservation of energy has not been addressed. The flow considered in this thesis is both isothermal and at low speed ($Ma < 0.3$), which greatly simplifies the analysis due to the assumptions of incompressibility² and constant density. By definition, incompressibility means that density is independent of pressure. It can, however, vary with temperature or composition of substances. At low speeds, $Ma < 0.3$, the fluid will behave as if it was incompressible, since the isentropic density change, ρ/ρ_0 , is less than 5% [2]. For a general flow problem, the equation of state expresses the change in pressure as a function of density and temperature, thus providing a linkage between the momentum and energy equations. With the assumptions of incompressible and isothermal flow, however, the density can be treated as constant, and the energy equation is decoupled from the system. The flow field can then be solved from continuity and momentum equations alone. Finally, neglecting gravitational acceleration and other body forces, the result is the following set of equations:

$$\frac{\partial u_i}{\partial x_i} = 0 \quad (2.4)$$

$$\frac{\partial u_i}{\partial t} + \frac{\partial}{\partial x_j} (u_i u_j) = -\frac{1}{\rho} \frac{\partial p}{\partial x_i} + \nu \frac{\partial^2 u_i}{\partial x_j^2} \quad (2.5)$$

The kinematic viscosity is by definition $\nu \equiv \frac{\mu}{\rho}$. To summarize, the analysis yields four equations for four unknown primitive variables; u , v , w and p .

The continuity equation and the Navier-Stokes equations expresses the physics that governs a fluid in motion, independent of the flow pattern or regime. Thus, both laminar and turbulent flow can be described by the above equations. In this sense, turbulence is, despite its chaotic nature, also a deterministic, yet complex solution to these equations. For laminar flow, only a few analytical solutions to extremely idealized cases exists. To solve for more complex flows involving turbulence, in practice all engineering computations, one must rely on numerical analysis.

²In the field of aero- and fluid dynamics, the term incompressibility is frequently used to express constant density. This is accepted practice, despite being technically incorrect.

2.3 A statistical approach

The instantaneous flow field will in this thesis be solved directly from equation (2.4) and (2.5) by means of DNS. This means that no assumptions or models are introduced in the equations being solved. However, to produce useful results and obtain statistically steady state quantities along with associated fluctuations, the flow field must be averaged in time (optionally in space for homogeneous directions). Exact transport equations for important turbulence quantities (see section 2.4) are also based on a statistical description of the flow field. Using such a decomposition of each flow variable is motivated by the fact that the practical interest in most cases lies in the large scale events, and not the small details. Hence, a formal definition of averaging is given.

2.3.1 Reynolds decomposition

As indicated before, the flow variables are decomposed into a mean and a fluctuating value. In a Reynolds decomposition, density is non-fluctuating, and the dependent variables, u_i and p , are decomposed as follows:

$$u_i = \bar{u}_i + u'_i \quad (2.6a)$$

$$p = \bar{p} + p' \quad (2.6b)$$

Here, the mean is defined in time³. That is, the mean value over a finite interval in time, Δt . This interval must be greater than the time scale of the smallest fluctuations, but at the same time smaller than the time scale of deviations in the mean value [20, p.35]. Here, ϕ is a general variable.

$$\bar{\phi}(x_i) = \frac{1}{\Delta t} \int_{t-\frac{1}{2}\Delta t}^{t+\frac{1}{2}\Delta t} \phi(x_i, t) dt \quad (2.7)$$

If the decomposed variables from equation (2.6) are inserted into the incompressible continuity and momentum equations, equation (2.4) and (2.5), governing equations for the mean flow will be obtained. These are called the Reynolds Averaged Navier Stokes equations (RANS). After some manipulation, the result yields that the mean flow properties satisfies continuity in the same way as before, but for the momentum equation, a new term occurs.

$$\frac{\partial}{\partial t}(\bar{u}_i) + \frac{\partial}{\partial x_j}(\bar{u}_i \bar{u}_j) = -\frac{1}{\rho} \frac{\partial \bar{p}}{\partial x_i} + \frac{\partial}{\partial x_j} (2\nu \bar{S}_{ij} - \overline{u'_i u'_j}) \quad (2.8)$$

The new term, $-\overline{\rho u'_i u'_j}$, is called the Reynolds stress tensor (RST)⁴. It is symmetric, and contains six unknown Reynolds stresses. These stresses represents the mean

³A Reynolds decomposition can also be an ensemble average.

transport of fluctuating momentum by turbulent velocity fluctuations [51, p.32]. Since the effect of turbulence on the mean flow field is now isolated into this term, it is of significant importance in the field of turbulence research and turbulence modelling.

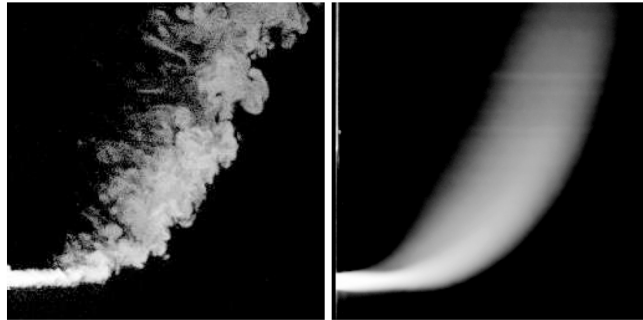


Figure 2.1: The effect of looking at the instantaneous or averaged flow field, respectively. From Durbin & Petterson-Reif [19].

2.3.2 Single-point closure methods

The vast field of turbulence modelling is concerned with closing the system of averaged equations for flow statistics, and basically it all comes down to different ways of handling the Reynolds stresses. Many models use an assumption which linearly relates RST to the mean strain rate, $-\overline{\rho u'_i u'_j} \propto \mu_T \overline{S_{ij}}$. This is in pure analogy to the linear stress-strain relationship in a Newtonian fluid. A so-called eddy viscosity, μ_T , is introduced as a proportionality factor. Another approach is to solve modelled transport equations for the Reynolds stresses alongside the continuity and momentum equations. Such second-moment closures⁵ (SMC), however, suffers from both an extreme increase in computational expense, and uncertainties in modelling of unclosed terms, especially the pressure-strain term, see equation (2.9).

2.4 Equations of turbulence

From the governing equations, presented in section 2.2, and by use of the introduced concept of Reynolds decomposition, equations for important turbulence quantities can be derived. Despite introducing averaged quantities into the derivation of the equations, the resulting equations are still exact, as they are only manipulated by mathematical operations [20, p.49]. However, they are unclosed, as correlations that are not exactly determinable occurs. Also, information about the instantaneous motions is filtered out and lost in the averaging process.

Even though this text is not concerned with solving these equations, nor the necessary modelling of terms, they describe fundamental mechanisms of turbulence

⁴It is consistent with literature that both $-\overline{\rho u'_i u'_j}$ and $\overline{u'_i u'_j}$ are referred to as RST.

⁵Also known as Reynolds Stress Modelling (RSM).

and highlights factors that govern the evolution of the mean flow. For DNS to be useful, post-processing of results is also highly concerned with calculating different terms so the importance and relevance of the different effects they represent can be quantified.

2.4.1 Second-moment equations

One way to derive an equation for the Reynolds stresses is to construct an equation for the fluctuation, $u'_i = u_i - \bar{u}_i$, from the momentum equations for the instantaneous and averaged velocities, u_i and \bar{u}_i respectively. The equation for u'_i is multiplied with u'_j , and a corresponding equation for u'_j is multiplied with u'_i . The two resulting equations are then added together and averaged [20, p.95]. The resulting transport equation is given as follows [20, p.95]:

$$\begin{aligned} \frac{\partial}{\partial t}(\overline{u'_i u'_j}) + \frac{\partial}{\partial x_k}(\overline{u'_i u'_j \bar{u}_k}) = & - \underbrace{\left(\overline{u'_i u'_k} \frac{\partial \bar{u}_j}{\partial x_k} + \overline{u'_j u'_k} \frac{\partial \bar{u}_i}{\partial x_k} \right)}_{P_{ij}} \\ & + \underbrace{\frac{\partial}{\partial x_k} \left(\nu \frac{\partial \overline{u'_i u'_j}}{\partial x_k} - \overline{u'_i u'_j u'_k} - \frac{1}{\rho} (\overline{p' u'_j} \delta_{ik} + \overline{p' u'_i} \delta_{jk}) \right)}_{d_{ij}} \quad (2.9) \\ & + \underbrace{\frac{p'}{\rho} \left(\frac{\partial u'_i}{\partial x_j} + \frac{\partial u'_j}{\partial x_i} \right)}_{\Phi_{ij}} - \underbrace{2\nu \frac{\partial u'_i}{\partial x_k} \frac{\partial u'_j}{\partial x_k}}_{\varepsilon_{ij}} \end{aligned}$$

The left side consists of a time derivative and an advection term, which is transport by the bulk flow. Terms on the right side are split into the effects they represent, production, diffusion and dissipation respectively. The production term, P_{ij} , describes transfer of energy from the mean flow to the fluctuations. From this term, it is easy to see that turbulence is only caused by, or generated from, shear in the mean flow. For most flows the production term is positive [19, p.50].

The second bracket, d_{ij} , is the diffusion and consists of four terms. The first and second are viscous (molecular) and turbulent diffusion respectively, while the two latter are pressure-diffusion. Their effect is to promote a spatial redistribution [37, p.13], but for many flows these terms are very small, or even negligible. For a channel flow, where there is no mean velocity gradient in the channel center, the contribution from this term provides turbulence to the center section.

The pressure-strain term, denoted Φ_{ij} , together with the pressure-diffusion terms originates from a term, which by terminology is called redistribution⁶ [19, p.53]. The pressure-strain is still redistributive, since the trace of Φ_{ij} is zero (due to continuity [17, p.77]). Hence, the term expresses a distribution of energy between

⁶In homogeneous turbulence, the redistribution- and pressure-strain terms are equal [19, p.53].

the Reynolds stress components, without affecting the overall energy balance. To be more precise, it can be shown that the effect is to make the turbulence more isotropic by transporting energy from the largest normal stresses to the ones being smaller [37, p.23-30]. Also, it acts as a sink, or a loss of correlation, on the Reynolds shear stresses [18, p.95].

The dissipation tensor, ε_{ij} , represents decay of turbulence, in other words dissipation due to viscous forces. For the normal stresses, $\overline{u'_i u'_i}$, we can say a drain of energy, but for the shear stresses, it is more precise to refer to a loss of $\overline{u'_i u'_j}$ -correlation.

It can be noted that the term being interpreted as dissipation in equation (2.9) is not equal to the exact viscous dissipation. This is also true for equation (2.11). However, the second part of the correct dissipation term has a much lower order of magnitude.

2.4.2 Turbulence kinetic energy budget

For a fluid in motion, the kinetic energy per unit mass is $\frac{1}{2}u_i u_i$. By subtracting the mean value of this quantity, and then take the average, the mean kinetic energy of the turbulent fluctuations, k , is obtained.

$$k \equiv \frac{1}{2}\overline{u'_i u'_i} = \frac{1}{2}(\overline{u'u'} + \overline{v'v'} + \overline{w'w'}) \quad (2.10)$$

By use of k , an energy budget for the turbulence can be established. Note that the turbulence energy is equal to half the trace of the Reynolds Stress Tensor, and by taking half the sum of the normal stresses from equation (2.9), the exact transport equation for the turbulence kinetic energy (TKE) is easily obtained [20, p.49]:

$$\frac{\partial k}{\partial t} + \frac{\partial}{\partial x_j}(k\bar{u}_j) = \underbrace{-\overline{u'_i u'_j} \frac{\partial \bar{u}_i}{\partial x_j}}_{P_k} + \underbrace{\frac{\partial}{\partial x_j} \left(\nu \frac{\partial k}{\partial x_j} - \frac{1}{2}\overline{u'_i u'_i u'_j} - \frac{1}{\rho}\overline{p' u'_j} \right)}_{d_k} - \underbrace{\nu \frac{\partial u'_i}{\partial x_j} \frac{\partial u'_i}{\partial x_j}}_{\varepsilon} \quad (2.11)$$

Naturally, this also implies the following relations; $P_k = \frac{1}{2}P_{ii}$ and $\varepsilon = \frac{1}{2}\varepsilon_{ii}$. On the left side of equation (2.11), the transient- and advection terms can be found. As for the RST equation, the effects of production, diffusion and dissipation are separated on the right side, but notice that the pressure strain term, Φ_{ij} , has vanished due to its redistributing property ($\Phi_{ii} = 0$). The first, P_k , is turbulence production. More precisely, what is actually meant by production is transfer of energy from the mean flow into the turbulence.

The three terms inside the bracket denoted d_k describes transport through diffusion. The first gradient term is transport of energy through viscous (molecular) mechanisms, thus called viscous diffusion. The two latter terms are connected to the turbulence motion, thereby called turbulent diffusion. In literature, they are

commonly referred to as a velocity-triple correlation and a pressure-velocity fluctuation. The last term is the viscous dissipation, ε , which still represents a loss of energy, or a decay of turbulence. From the smallest scales, energy is dissipated into heat.

2.5 The energy cascade and range of scales

In the so far presented theory on turbulence, some basic observations concerning the overall energy balance have been made. Terms describing production, or extraction of energy from the mean flow, different transport mechanisms, and losses due to dissipation have been identified. This whole process of transferring energy from large scales to small scales, across the intermediate scales, can be modelled as a cascade process. Commonly, this is referred to as the energy cascade of turbulence. The spectrum of eddies ranges from the largest integral scales, all the way down to the Kolmogorov micro scales, see figure 2.2.

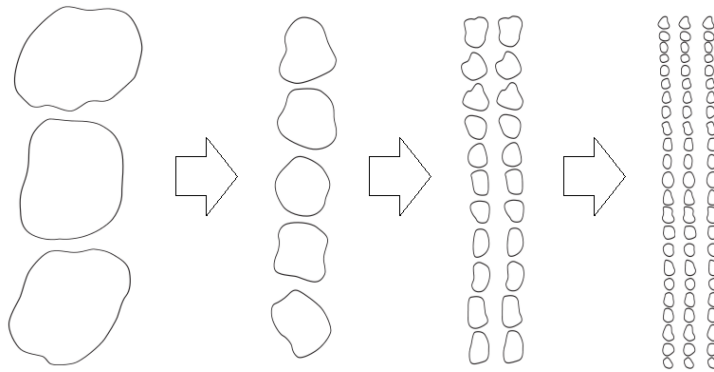


Figure 2.2: Through breakup and various processes such as vortex stretching of larger scale eddies, energy is transferred to continuously smaller scales. The breakup of eddies continues until viscous forces become dominant.

Now, characteristic scales for length, velocity and time are introduced for the larger energy-carrying eddies. A length-, velocity- and time-scale are denoted l_0 , u_0 and $\tau_0 = l_0/u_0$ respectively. Here, the dimension of l_0 is comparable to the length of the bounding geometry, L , and u_0 is comparable to the flow velocity scale U . Often, the square-root of the turbulence energy, $k^{1/2}$, is used to approximate u_0 . The Reynolds number for these eddies is therefore large, which means viscosity is negligible.

Under the assumption that mainly dissipation are important at the smallest scales, Kolmogorov developed expressions for the micro scales based purely on dimensional arguments. The assumption implies that the only influential quantities are the viscosity, ν , and the dissipation rate, ε . Different combinations of these quantities yields the Kolmogorov length-, velocity- and time scale respectively.

$$\eta = \left(\frac{\nu^3}{\varepsilon}\right)^{\frac{1}{4}} \quad u_\eta = (\nu\varepsilon)^{\frac{1}{4}} \quad \tau_\eta = \left(\frac{\nu}{\varepsilon}\right)^{\frac{1}{2}} \quad (2.12)$$

If the above expressions are used to form a local Reynolds number, the result yields $Re = 1$. Hence, inertia is balanced by viscous effects. At the end of the cascade-process, viscous stress dominates, and the mechanical energy is lost to heat.

From these expressions, useful scale relations can be obtained. First, the dissipation must be expressed by length and velocity scales of the large scale turbulence. Since the energy transfer is modelled as sequence of processes, it is argued that the rate of dissipation should be equal to the supply rate of energy from the large-scale eddies [51, p.20]. The kinetic energy per mass of the large scales is proportional to u_0^2 , and the rate of transfer of energy is assumed to be proportional to u_0/l_0 ($=\tau_0^{-1}$). Hence, the dissipation rate is of the order u_0^3/l_0 . Using equation (2.12), with the above dissipation rate, ε , the following can easily be obtained:

$$\frac{\eta}{l_0} = Re_0^{-\frac{3}{4}} \quad \frac{u_\eta}{u_0} = Re_0^{-\frac{1}{4}} \quad \frac{\tau_\eta}{\tau_0} = Re_0^{-\frac{1}{2}} \quad (2.13)$$

Here, $Re_0 = u_0 l_0 / \nu$ is the integral scale Reynolds number, which is comparable to the more familiar $Re = UL/\nu$. These relations can be useful parameters for the determination of required grid size and time step size in a DNS simulation. See e.g. Pope [46, p.347].

From the above dimensional argumentation, two features of turbulence can be emphasized. Firstly, the dissipation rate is primarily determined from large-scale dynamics. Secondly, the Kolmogorov scales are much smaller than the integral scales, as their relationships are all inverse proportional to Re_0 . Further, if Reynolds number is increased and the bounding geometry is kept constant (same integral scales), the only difference will be that the size of the smallest eddies will decrease and the fluctuations will become smaller and more rapid.

From a computational point of view, direct simulations has a very limited applicability, as the grid resolution should be smaller than the smallest effects in the flow, the Kolmogorov scales. As a consequence, DNS is limited to low or moderate Reynolds numbers.

2.6 Isotropic and homogeneous turbulence

Isotropic homogeneous turbulence is perhaps the simplest turbulent flow, but is rarely encountered in real-life applications. Isotropic turbulence means that the flow is statistically invariant to rotation of the coordinate system, while homogeneity means statistical invariance to translation of the coordinate system. For modelling applications, isotropy is important as the high Reynolds number hypothesis states that fine scale motions are unaware of the nature of the mean flow and large scale turbulence, thus the fine scale structure in any kind of turbulent flow is similar to

what is found in isotropic turbulence. In parallel shear flows, such as channel flow, the main source of anisotropy is the shear stress [19, p.155]. Near the walls, the Reynolds stresses, i.e. the velocity fluctuations, exhibits large anisotropy due to the presence of the wall.

A plane channel flow is homogeneous in streamwise and spanwise directions, and in terms of statistics, the flow field has a one-dimensional solution. When obstacles such as roughness elements is introduced, however, the flow becomes inhomogeneous also in the streamwise direction. Thus, statistical means are also dependent on streamwise location, and the solution becomes two-dimensional.

3 Channel flow with roughness

The following section contains a brief overview on rough-wall turbulence. Naturally, the introduction of surface roughness will have consequences for the near-wall boundary layer, and the structure of the turbulence in the region just above the roughness. Roughness is often encountered in practice, and many engineering problems cannot be regarded as hydraulically smooth.

From numerical studies, as well as laboratory experiments, turbulence- and flow data have been gathered over the recent years, and main findings for the relevant type of roughness is presented here. First, however, general concepts and theory on the effects of rough walls are given, together with a classification of roughness types.

3.1 A historical overview

In the field of fluid mechanics, surface roughness is a phenomena that has been subject to extensive research for almost two centuries. Some of the earliest studies, by Hagen and Darcy in the mid 19th century, was concerned with pressure loss in pipes. It was evident that the pressure drop increased drastically above a certain mass flow range, a finding that could indicate the presence of a different flow regime. In this regime, laminar theory was inadequate, and the problem was to link the friction factor to surface roughness.

In the beginning of the 20th century, Ludwig Prandtl and various students⁷ at the University of Göttingen, developed mathematical theories and identified phenomena related to aerodynamic lift, boundary layers, turbulence and laminar-turbulent transition. From this formidable group of researchers, Nikuradse [43] was left to evaluate the friction factor in pipes with wall roughness. The findings from his early sand-grain experiments are still considered to form the basis for rough-wall theory. For a given wall roughness, the correlation between flow Reynolds number and friction factor can be seen in [43, fig.9]. Now, such correlations can be found in the well-known Moody chart. Based on the work by Nikuradse, Schlichting [48] later introduced a concept of an equivalent sand-grain roughness parameter. For

engineering purposes, this quantity is widely in use today.

At NTNU, surface roughness has been a subject to experimental investigation over the last two decades, a lot of which has been published by professor Per-Åge Krogstad. In Krogstad & Antonia [35] and Antonia & Krogstad [3], different surface roughness geometries were investigated. In 2004, more effort was made to investigate a specific type of roughness. Both computational and experimental work on channel flow with transverse rib roughness was published in the doctoral theses of Ashrafiyan [4] and Bakken [8]. A comparative study between the results from DNS and experiments can be found in Krogstad et al. [34].

Reviews and comparative studies has also been published by Raupach et al. [47] and Jiménez [29].

3.2 Flow regimes

As mentioned above, Schlichting introduced the concept of an equivalent sand-grain roughness, k_s , which is the size of a sand-grain giving the same flow resistance as the surface geometry being investigated, at the same Reynolds number. This parameter then becomes a single descriptor for surface roughness, accounting for size, shape and density of the roughness elements [8, p.6], and is considered to be a *standard roughness*.

To characterize flow behaviour, two parameters are important: the roughness Reynolds number, k_s^+ , and the relative roughness [29, p.173], which is the ratio of roughness height to the characteristic boundary layer thickness. For a channel flow, the channel half-height is used. The roughness Reynolds number is introduced as $k_s^+ = k_s u_\tau / \nu$, where u_τ is the wall shear velocity, and ν the kinematic viscosity. Based on observations, different flow regimes can be identified [55, p.347]:

$$\begin{aligned} k_s^+ < 5 & : && \text{hydraulically smooth} \\ 5 \leq k_s^+ \leq 70 & : && \text{transitional roughness} \\ k_s^+ > 70 & : && \text{fully rough flow} \end{aligned} \tag{3.1}$$

These regimes are identified in the Moody chart, see figure 3.1. The hydraulically smooth line can be found in the bottom center of the diagram. Here, f is dependent on Re , but not on the relative roughness. In between this line and the dashed line to the right, the transitional roughness range is found. The friction factor depends on both Reynolds number and relative roughness, and both viscous and form drag are significant. For increasing Reynolds numbers to the right of the dashed line, the fully rough flow range is found. Here, friction factor is only dependent on relative roughness. This corresponds to a roughness Reynolds number of $k_s^+ > 70$, and flow resistance in this range is dominated by form drag.

⁷H. Schlichting, T. von Kármán, P. R. H. Blasius, W. Tollmien and J. Nikuradse are all well worth mentioning.

Note that the above flow regimes and corresponding limits, equation (3.1), is for the case of sand-grain roughness. In general, the critical limit depends on the geometric configuration [28, p.236], which means that a two-dimensional rod-roughness can have a critical limit significantly smaller. In Bandyopadhyay [9], it is shown that $r^+ \simeq 10$ is the critical limit for the fully rough state.

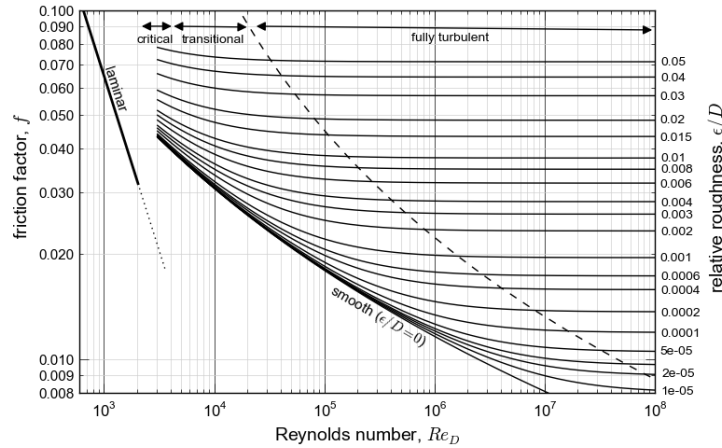


Figure 3.1: Moody chart for pipe friction factors. Here, the relative roughness is given by the roughness height, ϵ and the diameter of the pipe, D . Re is the Reynolds number based on bulk velocity.

3.3 Mean velocity profiles

Based on simple dimensional argumentation [19, p.59-60], some general considerations regarding the flow in the near-wall region can be made. First, suitable velocity- and length scales are chosen to normalize quantities. These are the wall shear velocity, u_τ , and the viscous length scale ν/u_τ . Using these wall units results in a set of *inner scaled* non-dimensionalized variables:

$$u^+ = \frac{\bar{u}}{u_\tau} \quad z^+ = \frac{u_\tau}{\nu} z \quad u_\tau = \sqrt{\frac{\tau_w}{\rho}} \quad (3.2)$$

3.3.1 The wall region

The region $z^+ \lesssim 100$ is considered the *wall region*, and is divided into different layers based on which forces are dominating. The region adjacent to the wall, $z^+ < 5$, is relatively insensitive to the outer flow, and viscous forces are dominating. In this *viscous sublayer* the velocity is simply a linear function of the wall distance; $u^+ = z^+$. Further away, in the so-called logarithmic region, $z^+ > 30$, turbulent shear is dominating. The velocity is found to vary logarithmically according to the log-law, or law of the wall:

$$u^+ = \frac{1}{\kappa} \ln z^+ + A \quad (3.3)$$

The constant κ is determined from experiments, and takes the universal value $\kappa \approx 0.41$ [54, p.417]. For a smooth wall, Nikuradse [43] suggested $A \approx 5.5$ based on his experiments, but later correlations suggests $A \approx 5.0$ to be used instead [54, p.417].

In between the two above mentioned regions, both viscosity and turbulence effects are influential, and none of the above relations holds entirely. This regions is called the *buffer layer*, and the velocity profile smoothly connects the regions. For a smooth wall, figures 5.2 and 5.5 in chapter 5 shows the velocity profile and distribution of shear respectively.

3.3.2 The outer layer

For $y^+ > 100$, we normally speak of an *outer layer*. Here, u_τ together with the channel half-height, δ , is used to form an *outer scaling*. The velocity profile is described by the *velocity defect law*, given as:

$$u_{CL}^+ - u^+ = -\frac{1}{\kappa} \ln \left(\frac{z}{\delta} \right) + K \quad (3.4)$$

u_{CL}^+ is the channel centerline velocity, the term $u_{CL}^+ - u^+$ is the retardation of the flow due to wall effects [54, p.416] and K is a constant. In contrast to equation (3.3) which must be modified for wall roughness, equation (3.4) is valid for both smooth and rough surfaces [15, 34]. This indicates some similarity between smooth- and rough wall boundary layers in the outer layer. This has however been questioned by Krogstad et al. [36], where it was observed that the constant K was not the same for smooth and rough boundary layers (see *wall similarity hypothesis*, section 3.5).

3.3.3 Mean velocity scaling

From the previously mentioned experiments of Nikuradse, it was found that there is a shift outwards and downwards in the velocity profile, as illustrated by figure 3.2. The logarithmic slope, however, remains the same. In a channel flow with a given pressure drop, the mass flux must decrease due to the increased drag force, and thus the constant B_s in equation (3.3) must decrease [19, p.63]. Thus, the smooth wall relation is modified to the form [34, p.328]:

$$u^+ = \frac{1}{\kappa} \ln \left(\frac{z}{r} \right) + B(r^+) , \quad B(r^+) = A - \Delta u^+ + \frac{1}{\kappa} \ln r^+ \quad (3.5)$$

Here, subscript r in B_r indicates that the additive constant is for the rough surface. r is the roughness length scale, in the case for sand grain-roughness equal to k_s and for rod- roughness the height of the roughness elements, r . r^+ is the roughness

Reynolds number, non-dimensionalized using the viscous length scale ν/u_τ (same as for k_s^+). Also note that the length scale used to normalize z , is different from what is used in the smooth-wall relation, equation (3.3). The new variable, $B(r^+)$, is dependent on the roughness Reynolds number, and is expressed by introducing the so-called *roughness function*, Δu^+ , as equation (3.5) shows. For sand-grain roughness, the shift is given by [34, p.328]:

$$\Delta u^+ = +\frac{1}{\kappa} \ln k_s^+ + A - C \quad (3.6)$$

Nikuradse reported that $C \approx 8.5$ for the fully rough flow regime. For other roughness types, it might be useful to relate the roughness length scale r to the equivalent sand-grain roughness length scale k_s . Once Δu^+ is known, the relation is given by [34, p.328]:

$$\frac{k_s}{r} = \frac{\exp[\kappa(\Delta u^+ - A + C)]}{r^+} \quad (3.7)$$

Figure 3.2 shows the shift, Δu^+ , in mean velocity profile produced by the surface roughness.

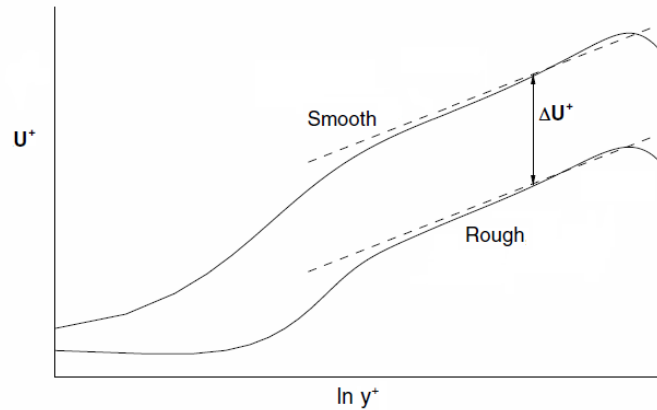


Figure 3.2: Shift in mean velocity profile. Figure from Ashrafiyan [4].

3.4 Roughness classifications

In real life, surface roughness has a highly random and complex shape, which for engineering purposes is represented by the one descriptive parameter, k_s . In numerical simulations and partly laboratory experiments, efforts can however be made to study particular shapes of roughness. For the present case, spanwise rectangular ribs are appended to the walls as a simple roughness model. This thesis, and the results discussed in this chapter will from here on mostly be concerned with this configuration.

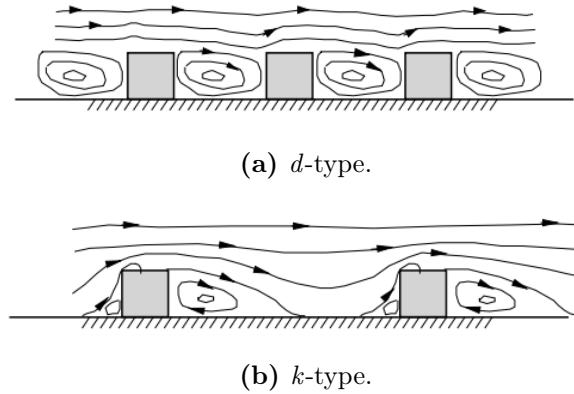


Figure 3.3: Surface roughness classification. Figures from Ashrafian [4].

In Raupach et al. [47] the above mentioned roughness model is classified as a 2-D roughness case. Further, for such a configuration, two types of roughness exists, one allows for formation of stable vortices in the cavities, while the other is characterized by unstable eddies behind the elements, see figure 3.3. The terminology *d*- and *k*-type roughness are used respectively. For *d*-type roughness, the spacing between the ribs, denoted w , is in the order of the element height, while for *k*-type the spacing is somewhat larger, $w/r > 3$ is suggested by Bandyopadhyay [9]. The roughness height, in this case the height of the elements, is denoted r .

For this two-dimensional roughness, the pitch-to-height ratio, $\lambda = p/r$, is an important parameter. See figure 4.2 in section 4.4.1. The effect of roughness is found to be largest for $5 < \lambda < 9$ by Furuya et al. [23] and also in a DNS-study by Leonardi et al. [39]. Hence, the largest shift in velocity profile is found in this range of λ -ratios. For $\lambda > 10$, the roughness effect was found to decrease.

The generation of stable vortices, or pockets of recirculating fluid in the cavities in the *d*-type case effectively results in a decrease in overall drag force compared to a smooth wall [39]. The main flow now partly interacts with the fluid in the cavities and partly the top of the roughness elements, hence the total shear force resistance is reduced. Further, if the height of the roughness elements becomes to high, and at the same time, spacing is sufficiently large, the object will no longer be considered as roughness, instead the case will be a flow around an obstacle (bluff body). Comparing the roughness height to the characteristic length of the boundary layer, the ratio r/δ should not exceed 0.025 [29]. Keeping the ratio below this value will eliminate direct effects on the outer flow.

3.5 The roughness sublayer and wall similarity

In general, the effect of roughness is well understood for the mean velocity profile in near-wall layers, but how other turbulence features and structures are affected, especially in the outer layer, has been more controversial [10, p.463], and perhaps

not fully understood.

Adjacent to the wall, there exists a roughness sublayer, typically stretching out to a distance of 3 to 5 roughness heights [34]. However, as stated by Bhaganagar et al. [10], this distance depends on the shape and density distribution of the introduced roughness. In this inner layer, the dominant flow structures have length scales of the order of the roughness elements, and the intensity of velocity and vorticity fluctuations are significantly increased by the roughness. Also, the elements interact strongly with the near-wall streamwise vortices.

Generally, it has been assumed that the roughness will have no or little influence on the outer layer turbulence. This was first posted by Townsend [52], then modified by Perry & Abell [44], as the *wall similarity hypothesis*. It states that turbulent motions are independent of the details of the wall roughness at sufficiently large Reynolds numbers, i.e. that smooth and rough wall turbulence is similar outside the roughness sublayer. This has been confirmed and used by many researchers, for both 2-D and 3-D roughness. Among these are the experiments of Perry et al. [45] and laboratory and atmospheric data from Raupach et al. [47]. However, the hypothesis has been questioned by Krogstad et al. [36] for boundary layer flow. They found several structural differences also in the outer region. Experimental results from Krogstad & Antonia [35] also question whether the hypothesis actually holds.

To proceed, a note on boundary layer flow (external flow) and channel flow (internal flow) should be given. In rough-wall turbulence research, both flow-types have been thoroughly investigated. Despite displaying many of the same features, there are however some fundamental differences pointed out by various researchers that partly can explain discrepancy from the wall similarity. It is noted that issues in determining friction velocity correctly in the experimental results of Krogstad et al. [36] and Krogstad & Antonia [35] could lead to a high degree of uncertainty [34]. Length scales associated with channel flows are constant in the streamwise direction, while characteristic lengths in external flows are changing with boundary layer thickness. Also, channel flows are always driven by a favourable pressure gradient, which in turn leads to a reduced wake strength. This makes the velocity defect profile more likely to be similar for rough and smooth walls in channel flows [34]. Jiménez [29] also notes that there are differences in wall normal transport of TKE. In channel flow, turbulence energy is transported to the channel center by diffusion, where it counteracts the dissipation (as noted in section 2.4.1). In boundary layer flow, other mechanisms are present, and part of the energy is also used to support boundary layer growth. All together, these differences might suggest that internal and external flows over rough walls behave different [34].

Having the above mentioned differences in mind, it is suggested by some that rough-wall boundary layers can be categorized according to whether the surface roughness affects the outer layer or not [10, p.465]. Further, it may be that the nature of some surfaces are that they "communicate" with the outer layer, while others do not. This difference in layer-interaction can still exist, even though two surfaces share the same characteristics such as height or density, and even if they produce the same lower-order statistics (e.g. shift in mean velocity profile). Jiménez [29]

also concludes in his review that the matter of turbulent structure and interaction between layers is far from understood, as there are conflicting experiments in almost all cases.

3.6 Numerical simulation

Over the recent years, channel flow with transverse rib roughness has been investigated using both DNS and LES. As mentioned, Bandyopadhyay [9] suggests that critical value for the fully rough flow regime is $r^+ \simeq 10$ for 2-D rod-roughness, hence most of the results are obtained for fully rough flow. Further, many of the below simulations are motivated by the experiments of Hanjalic & Launder [27], and produces an asymmetric flow field, due to roughness elements used only at one wall. The roughness heights are all in the range of 10% – 20% of the channel half-height, δ , thus there may be a significant blockage effect. Roughness heights in this range are also much higher than what was proposed as a maximum by Jiménez [29]; $r/\delta \leq 2.5\%$.

Ikeda & Durbin [28] performed DNS of a channel having transverse ribs mounted on one side, while the other wall remained smooth. The Reynolds number was $Re_\tau = 460$ based on the smooth wall friction velocity, and for the k -type roughness, a pitch-to-height ratio of 10 was used. The height of the elements corresponded approximately to $r^+ = 110$. Their study was aimed at the investigation of TKE-flux in the roughness sublayer. For surface roughness, the wall-normal coordinate origin, $z = 0$, can be defined at the mean height of the roughness elements [28, p.235], which means that the turbulent kinetic energy is not zero at $z = 0$. In this sense, the rough surface acts as a sink or source for TKE. Ikeda & Durbin [28] found a significant turbulence energy flux in the roughness sublayer, and that vortical structures is responsible for a high energy production in this region.

Leonardi et al. [39, 38] used a similar setup with square bars on one wall in a turbulent channel flow using DNS. Here, several pitch-to-height ratios ($\lambda = 2, 4, 8, 20$) were investigated. The bulk Reynolds number was held constant at 4200, which means a constant flow rate was used. Re_τ ranged between 190 ($\lambda = 1$) and 460 ($\lambda = 8$). r^+ was in the range 40 to 90. They verified that the roughness function, Δu^+ , was only dependent on r^+ , and not the Reynolds number for $r^+ \geq 10$, which means that this corresponds to the fully rough flow regime. This supports what was suggested by Bandyopadhyay [9] as a critical limit for this particular roughness type.

Simulations using LES has, among others, been performed by Cui et al. [16], at a bulk Reynolds number of $Re_b = 10\,020$, based on channel half-height. Both d - and k -type roughness were investigated, where the k -type had a pitch-to-height ratio of 10, and roughness height was 20% of the channel half height. They observed a limit for d -type roughness at $\lambda = 5$, and found that roughness having pitch-to-height ratios just above this limit led to strong interaction between the inner and outer layer.

Bhaganagar et al. [10] used DNS to simulate flow over a one side three-dimensional "egg carton" shape. Different roughness heights were simulated; $r^+ = 5.4, 10.8, 21, 6$ at $Re_\tau = 400$. They found that the downwards shift in mean velocity profile corresponded well with what was reported by Raupach et al. [47]. Also, the strength of the inner and outer layer interaction was greatly affected by the size of roughness elements.

For two-side rib-roughness, DNS and experimental results are available from Ashrafiyan [4] and Bakken [8], who were among the first to study such a configuration. The Reynolds number was $Re_\tau = 400$ in the DNS, and $Re_\tau = 600$ in the experiment. Here, the wall shear velocity could be calculated from the mean pressure gradient due to the symmetric channel configuration. The roughness height in the DNS was 0.034 of the channel half-height, which corresponds to $r^+ = 13.6$ ($r^+ = 20.4$ in the experiment). In the outer region, the velocity defect plot indicated that there is no influence of surface roughness. Thus, the results generally supports the wall similarity hypothesis [34, p.23]. Further, the Reynolds stresses was similar outside $z^+ = 5r^+$, but the turbulence structure seemed to be somewhat more affected in this outer region. Compared to the study of Leonardi et al. [39], the low value of $r^+ = 13.6$ explains why the results are rather different, despite having the same pitch-to-height ratio.

4 Numerical approach

In chapter 2, equations governing the fluid motion were presented. This chapter addresses the issues of solving the equations on the computational domain and employing the correct physical constraints on the boundaries. Further, full structure of the code is not presented in detail, but main features such as solution techniques and numerical schemes are discussed briefly.

A pseudo-spectral DNS computer code originating from Prof. Boersma and Dr. Gillisen at TU Delft is used in the simulations [24, 26]. The code is written in FORTRAN language, and parallelized using Message Passing Interface (MPI). Originally, it was used to study fibre-induced drag reduction in plane channel flow. The code has been verified, validated and used extensively by various researchers [24, 26, 25, 56] for the above mentioned purpose. Later, a small extension to include wall roughness was made by Dr. Zhao at NTNU, but the code was never properly tested for this.

Note that i and k in the present chapter can have various meanings to be consistent with common practice in literature.

4.1 Direct Numerical Simulation

In a direct simulation, all turbulent scales are resolved. The computational cost is highly dependent on both spatial grid resolution and the required number of time steps, two parameters that are directly related to the Reynolds number, Re . Using the relations from equation (2.12) and (2.13), it can be shown that the total number of required grid points, $N = N_x N_y N_z$, grows with $Re^{3/4}$. At the same time, the number of time steps grows with $Re^{1/2}$ [19, p.307]. This means that a total approximation of floating point operations required scales to $Re^{11/4}$. Obviously, this makes DNS limited to quite moderate Reynolds numbers.

In the beginning, direct simulations were limited to fully isotropic, homogeneous turbulence, using spectral methods for efficiency. Now, finite difference schemes, or a combination of finite difference and spectral schemes, such as the code used in this thesis, are typically used. As computational resources has become more available,

DNS is also used to simulate more complex flows involving compressibility and combustion.

In the present DNS, the governing equations are solved in a non-dimensionalized form:

$$\frac{\partial u_i^*}{\partial x_i^*} = 0 \quad (4.1)$$

$$\frac{\partial u_i^*}{\partial t^*} + \frac{\partial}{\partial x_j^*}(u_i^* u_j^*) = -\frac{\partial p^*}{\partial x_i^*} + \frac{1}{Re_\tau} \frac{\partial^2 u_i^*}{\partial x_j^{*2}} \quad (4.2)$$

where the non-dimensionalized variables are defined as follows:

$$u_i^* = \frac{u_i}{u_\tau} \quad x_i^* = \frac{x_i}{h} \quad t^* = \frac{tu_\tau}{h} \quad p^* = \frac{p}{\rho u_\tau^2} \quad (4.3)$$

Note that in all following sections in the present chapter, we are still solving for non-dimensionalized variables, but the star superindex is not written to avoid writing too many indices.

4.2 Pressure-velocity coupling

The Navier-Stokes equations is a coupled system of equations for the velocities and pressure, and main difficulties in solving these equations arises from the fact that no explicit equation for the pressure exists. For the incompressible case, the continuity equation also lacks both a dominant variable and a time-derivative, thus it acts as an additional kinematic constraint on the velocity field instead of being a dynamic equation [22, p.167]. In an unsteady calculation, the pressure at each time-step must then adapt in such a way that mass conservation is satisfied.

The system can be solved as a fully coupled problem, explicit, implicit or semi-implicit in time, but a more efficient method for the case of incompressibility is to use a fractional step method⁸. This is a variant of pressure projection methods commonly used in fluid dynamics, and implies that the velocity and pressure fields are decoupled and solved separately. For each time step, simpler sub-problems are solved. The basis for such solution methods is a Helmholtz decomposition of the vector field into the sum of one part with zero curl and one part with zero divergence [14, p.746].

The fractional step method used in fluid dynamics, originally proposed by Chorin [14] and Temam [50], first estimates an intermediate, non divergence-free velocity field at the beginning of each new time-step without taking pressure into account. Then, pressure is calculated from a constructed Poisson equation that, in addition

⁸Also called operator splitting methods or segregated methods in various literature.

to provide the pressure, also enforces mass conservation. Finally, velocities are updated using the calculated pressure.

4.3 Discretization

The equations are discretized and solved on a Cartesian grid that is non-uniform in wall-normal direction. In streamwise and spanwise directions, velocities u and v are stored in the cell-center point. This is also the case for the pressure. In wall-normal direction, a staggered configuration is used, which means velocities w are stored at cell faces. Such a configuration is often advantageous due to stronger coupling between velocity and pressure [22, p.166].

Further, a pseudo-spectral method is used for the streamwise and spanwise derivatives. This is primarily motivated by efficiency, as computation of derivatives in Fourier space⁹ is highly accurate and simple. Also, the Fourier coefficients converges exponentially when the number of collocation points approaches infinity. Compared to the central differencing scheme, it can be shown that a spectral method with N collocation points is more accurate than the former using $2N$ points [21, p.85]. However, use of this particular method requires FFT-algorithms to be used, which in turn is only available to equi-spaced points [21, p.87].

For the discretized Navier-Stokes equations, all spatial derivatives in the x - and y -momentum equations are approximated around the u, v velocity point (cell center), while the z -momentum equation is approximated around the w -velocity point (cell face).

As pointed out in various literature, e.g. by Ferziger [21, p.86], the error resulting from spatial and temporal discretization should be balanced, i.e. of the same order. If this is not the case, the simulation is probably run at a too high cost. In the present case, the time advancement scheme and the wall-normal central differencing scheme is second order accurate.

4.3.1 Time advancement

Temporal discretization, or time stepping, is carried out using the methodology described in section 4.2 with an explicit second-order Adams-Bashforth (AB2) scheme. In general form, this two-step method is given as

$$y_{n+1} = y_n + h \left(\frac{3}{2}f(t_n, y_n) - \frac{1}{2}f(t_{n-1}, y_{n-1}) \right) \quad (4.4)$$

The two constants can easily be found from Taylor expansion. n denotes the current time step, y_{n+1} is the approximation of the solution at time-step $n + 1$ and h is the time step-size. The above scheme is employed for the time derivatives of the

⁹*Fourier-, spectral- and wavenumber-space* are used interchangeably in literature.

velocities, both for advection and viscous terms¹⁰. The same cannot be done for pressure, since no time derivative exists. The pressure is simply chosen to be treated implicitly in time, that is, evaluated at the next time-step. Approximation of spatial derivatives can be of any order and any type, but for now they are simply denoted as δ_i ($= \delta/\delta x_i$) and δ_i^2 ($= \delta^2/\delta x_i^2$). Inserting the above scheme into equation (4.2) yields the time-discretized Navier-Stokes equations:

$$\begin{aligned} \frac{u_i^{n+1} - u_i^n}{\Delta t} &= \frac{3}{2} \left(-\delta_j(u_i^n u_j^n) + \frac{1}{Re_\tau} \delta_j^2 u_i^n \right) \\ &\quad - \frac{1}{2} \left(-\delta_j(u_i^{n-1} u_j^{n-1}) + \frac{1}{Re_\tau} \delta_j^2 u_i^{n-1} \right) - \delta_i p^{n+1} \end{aligned} \quad (4.5)$$

By rewriting the above equation, an expression for the intermediate, non divergence-free velocity field can be constructed. This velocity field, $u_{i\star}^{n+1}$, is only dependent on previous time-step velocities.

$$\begin{aligned} u_i^{n+1} + \Delta t \delta_i p^{n+1} = u_{i\star}^{n+1} &= u_i^n + \Delta t \left[\frac{3}{2} \left(-\delta_j(u_i^n u_j^n) + \frac{1}{Re_\tau} \delta_j^2 u_i^n \right) \right. \\ &\quad \left. - \frac{1}{2} \left(-\delta_j(u_i^{n-1} u_j^{n-1}) + \frac{1}{Re_\tau} \delta_j^2 u_i^{n-1} \right) \right] \end{aligned} \quad (4.6)$$

To proceed further, one can take the numerical divergence of equation (4.6). Mass conservation at the next time-step is enforced by $\delta_i u_{i\star}^{n+1} = 0$ (follows from the continuity equation). Pressure at the new time-step can then be calculated from the following, discrete, Poisson problem:

$$\frac{\delta}{\delta x_i} \left(\frac{\delta p^{n+1}}{\delta x_i} \right) = \frac{1}{\Delta t} \frac{\delta}{\delta x_i} (u_{i\star}^{n+1}) \quad (4.7)$$

The Poisson equation results in a linear system of equations (a three-band matrix), which is solved using a conventional tri-diagonal matrix solver [24, p.39]. Updated, end-of-step velocities are finally found by going back to equation (4.6) using the pressure from equation (4.7). As stated earlier, a Fourier basis is used to compute derivatives in x and y directions, hence equation (4.7) is transformed, and solved in Fourier-space in these directions [24, p.30].

The introduction of equation (4.7) also demands one additional boundary condition for the pressure than what was originally required by the system. Thus, equation (4.7) should be supplemented by a Neumann boundary condition. This, however, can lead to issues concerning the behaviour of the pressure at the walls. This topic has been addressed by many authors, most recently a review was given by

¹⁰For stability reasons [13, p.148], it can be favourable to treat viscous terms implicitly, e.g. by a Crank-Nicholson scheme, as in the fractional step method by Kim & Moin [31].

Vreman [53]. For this particular code, it can be shown that the introduced boundary condition leads to a correct velocity field, while no further effort is paid to precisely compute the pressure [24, p.31].

At last, note that the two-step AB2 scheme is not self starting because of the u_i^{n-1} terms.

4.3.2 Spatial derivatives- streamwise and spanwise directions

Streamwise and spanwise derivatives are computed in Fourier space using a pseudo-spectral method. The velocities, u_i , are replaced with a Fourier series expansion, and fast Fourier transform algorithms (FFT or FFT⁻¹) are used to transfer the variables between physical space and Fourier space.

Since we are dealing with numerical computer computations, the values are evaluated at n discrete grid points, or collocation points. A complex Fourier series for the function $u(x_n, t)$ (physical space) then becomes [12, p.47-48]:

$$u(x_n, t) = \sum_{k=-\frac{N}{2}}^{\frac{N}{2}-1} \hat{u}_k(t) e^{ik\frac{2\pi}{L}x_n}, \quad n = 0, 1, 2, \dots, N-1 \quad (4.8a)$$

$$\hat{u}_k(t) = \sum_{n=0}^{N-1} u(x_n, t) e^{-ik\frac{2\pi}{L}x_n}, \quad k = -\frac{N}{2}, \dots, \frac{N}{2}-1 \quad (4.8b)$$

where $\hat{u}_k(t)$ (Fourier space) is the Fourier coefficients calculated by the FFT-algorithm, i is the imaginary number, k the wavenumber ($k = L/\lambda$) and L the period, i.e. the domain length. Note that the highest wavenumber that can be represented (captured) by N grid points is $k_{max} = \pi/\Delta x = N/2$ [46, p.345].

A key property of the Fourier transform [33, p.522]¹¹ is that evaluation of first- and higher order derivatives in Fourier space is a straight forward multiplication operation, due to the Fourier-basis e^{ikx} . Effectively, this creates a new set of Fourier-coefficients for the derivatives, i.e. $\hat{u}'_k = ik\hat{u}_k$. From this it follows that the exact derivatives in the collocation points can be calculated from the following [12, p.52]:

$$\frac{d}{dx}u(x_n, t) = \sum_{k=-\frac{N}{2}}^{\frac{N}{2}-1} \frac{2\pi}{L} ik\hat{u}_k(t) e^{ik\frac{2\pi}{L}x_n}, \quad n = 0, 1, 2, \dots, N-1 \quad (4.9a)$$

$$\frac{d^2}{dx^2}u(x_n, t) = \sum_{k=-\frac{N}{2}}^{\frac{N}{2}-1} -\left(\frac{2\pi}{L}k\right)^2 \hat{u}_k(t) e^{ik\frac{2\pi}{L}x_n}, \quad n = 0, 1, 2, \dots, N-1 \quad (4.9b)$$

In the above equations, the time-dependency can also be removed since time advancement is carried out in physical space, see section 4.3.1.

¹¹Theorem 3: $\mathcal{F}\{u'(x)\} = ik\mathcal{F}\{u(x)\}$. \mathcal{F} is the Fourier-transform.

Most algorithmic complexities in spectral methods comes from non-linear terms [13, p.99], which in this case is the advection term in the Navier-Stokes equations. The name "*pseudo-spectral*" refers to a special way of computing this term. Evaluating this in Fourier space is extremely computer demanding due to the number of operations required to evaluate the convolution sum, $\mathcal{O}(n^2)$ [12, p.132]. To avoid this, non-linear terms are solved by going back to physical space where multiplication is straight forward. This means that the individual coefficients, say \hat{u}_k, \hat{v}_k , are first transformed back into physical space (FFT⁻¹), multiplied to form a new function, $s_n = u_n v_n$, and finally transformed back to Fourier space (FFT) where differentiation is performed as described above, $\hat{s}'_k = ik\hat{s}_k$. By doing this, the required number of operations for one spatial direction is reduced from the order $\mathcal{O}(n^2)$ to that of FFT, namely $\mathcal{O}(n \log n)$ [12, p.133].

4.3.3 Spatial derivatives- wall-normal direction

In z -direction, second order accurate central differencing schemes are used to calculate first- and second order derivatives. The schemes account for both the staggered configuration and the non-uniform grid spacing. Note that the schemes are written in general form, which means that the variable u in the schemes can either be u, v, w or p . Further, i is used as grid cell index, and indices f and c denotes cell face and center respectively (see figure 4.4). Schemes for first-order derivatives reads as follows:

$$\left. \frac{\partial u}{\partial z} \right|_{z_i^c} \approx \frac{u_i^f - u_{i-1}^f}{z_i^f - z_{i-1}^f} \quad (4.10a)$$

$$\left. \frac{\partial u}{\partial z} \right|_{z_i^f} \approx \frac{u_{i+1}^c - u_i^c}{z_{i+1}^c - z_i^c} \quad (4.10b)$$

A central, second order accurate scheme for the second derivative is found by successive use of the above schemes:

$$\left. \frac{\partial^2 u}{\partial z^2} \right|_{z_i^c} \approx \frac{\left. \frac{\partial u}{\partial z} \right|_{z_i^f} - \left. \frac{\partial u}{\partial z} \right|_{z_{i-1}^f}}{z_i^f - z_{i-1}^f} \quad (4.11a)$$

$$\left. \frac{\partial^2 u}{\partial z^2} \right|_{z_i^f} \approx \frac{\left. \frac{\partial u}{\partial z} \right|_{z_{i+1}^c} - \left. \frac{\partial u}{\partial z} \right|_{z_i^c}}{z_i^c - z_{i-1}^c} \quad (4.11b)$$

For the calculation of first derivatives and non-linear terms, velocities need to be interpolated between cell faces and centres. A simple linear interpolating scheme reads:

$$u_i^f = \frac{1}{2}(u_{i+1}^c + u_i^c) \quad (4.12a)$$

$$u_i^c = \frac{1}{2}(u_i^f + u_{i-1}^f) \quad (4.12b)$$

The nonlinear terms are evaluated in the same way as given by equation (4.10), but uw , vw and wv must of course be evaluated in the same grid point. For the z -derivatives of non-linear terms in x - and y -momentum equations, approximations are around the cell-center point, which means u and v are first interpolated to the cell faces using equation (4.12). As an example, for uw , the resulting scheme can be written:

$$\left. \frac{\partial}{\partial z}(uw) \right|_{z_i^c} \approx \frac{\left(\frac{1}{2}(u_{i+1}^c + u_i^c)w_i^f \right) - \left(\frac{1}{2}(u_i^c + u_{i-1}^c)w_{i-1}^f \right)}{z_i^f - z_{i-1}^f} \quad (4.13)$$

Note that in the code [11], z_i^f and z_i^c are stored in the vectors R_w and R_p respectively.

4.3.4 Stability

The explicit AB2 scheme is only conditionally stable, which means stability can only be achieved for some values of Δt for a given spatial resolution. Construction of a stability criterion for the entire Navier-Stokes equations is not straight forward, but a basis can be formed by evaluating inviscid terms (advection-equation; hyperbolic) and viscous terms (diffusion-equation; parabolic) independently. For either of these time-dependent modelling equations, the standard CFL-conditions read [1, p.68,85]:

$$CFL_{\text{adv}} = \Delta t \frac{|u|}{\Delta x} \leq C_{1,\text{max}} , \quad CFL_{\text{diff}} = \Delta t \frac{1}{\nu \Delta x^2} \leq C_{2,\text{max}} \quad (4.14)$$

where the Courant numbers $C_{1,\text{max}}$ and $C_{2,\text{max}}$ are dependent on spatial and temporal discretization schemes. By combining the above expressions, a maximum allowed Δt is calculated as follows for the fully three-dimensional case [11]:

$$\Delta t_{\text{max}} = C_{\text{max}} \left[\left(\frac{|u|}{\Delta x} + \frac{|v|}{\Delta y} + \frac{|w|}{\Delta z} \right) + \frac{1}{Re_\tau} \left(\frac{1}{\Delta x^2} + \frac{1}{\Delta y^2} + \frac{1}{\Delta z^2} \right) \right]^{-1} \quad (4.15)$$

where $C_{\text{max}} = 0.3$ [11]. Note that the condition expressed by equation (4.15) is necessary, but may not be sufficient for the numerical discretization to be stable. To monitor the stability, Δt_{max} is calculated for each cell at each time-step, and the limiting value, $\max \Delta t_{\text{max}}$, is written to a monitor file.

4.3.5 Aliasing error

An issue arising from using the pseudo-spectral method for the non-linear terms is the generation of an aliasing error. A calculation of a convolution sum, where two

Fourier-coefficients are multiplied, generates wavenumbers higher than what can be resolved on the grid ($k > N/2$) [19, p.320]. The highest wavenumber generated, k_{max} , is equal to N . Thus, this sum should be truncated, so high wavenumbers are left out. However, using the pseudo-spectral evaluation, no truncation of the sum occurs. Instead, these high wavenumber signals can be misinterpreted as having a lower wavenumber similar to those within the computational range, see figure 4.1. This can significantly corrupt the simulation by causing numerical instability or excessive turbulence decay [40, p.545], as observed by Kim et al. [32]. Especially, this is the case for wavenumbers just above $N/2$, while aliasing from high N might not be harmful, since the turbulent energy spectrum has a low amplitude for high wavenumbers [19, p.321].

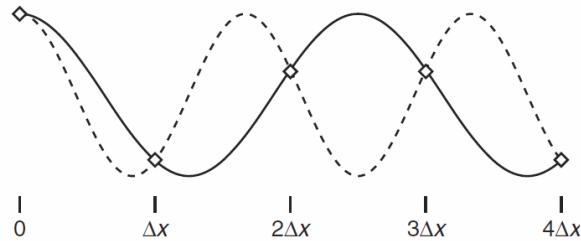


Figure 4.1: The high wavenumber signal (dashed line) has a lower-frequency alias (continuous line), since the two signals are indistinguishable at the collocation points. From Durbin & Petterson-Reif [19, p.321].

The simplest way to de-alias results, is to use a standard 3/2 rule [19, p.321]. In Fourier space, the series are first extended by adding Fourier-coefficients in the range $N/2$ to $3/4N$. Then, the product is formed in physical space on a grid with a spacing of $2/3\Delta x$, i.e. at $3/2N$ collocation points. When transformed back to Fourier-space, modes beyond $N/2$ is deleted [19, p.321]. In this way, the computational range is uncontaminated.

4.4 Simulation setup

In the simulations, the approach of keeping the wall friction Reynolds number constant is used. Hence, for both the smooth and the rough channel, the wall friction Reynolds number $Re_\tau = u_\tau \delta / \nu$, is prescribed. For the smooth channel, $Re_\tau = 180$, and for the rough channel $Re_\tau = 395$ is set. These Reynolds numbers are chosen based on what is available for comparison. Here, it can also be noted that in the code, different variables scales with the channel height, h , while most literature use the channel half-height, δ . The code input is therefore $Re_{\tau,h} = 360$, $Re_{\tau,h} = 790$, and $-dp^*/dx^* = 2$, where $Re_{\tau,h}$ is the friction Reynolds number based on channel height, h .

For a symmetric channel configuration, such as the channel having two side roughness, u_τ is directly related to the pressure drop through the wall friction [34]:

$$-\frac{dp^*}{dx^*} = \frac{\tau_w}{\delta} = \frac{u_\tau^2 \rho}{\delta} \quad (4.16)$$

At the same time, this friction velocity used for scaling is the same for both walls. The symmetric channel implies that the mean velocity field and turbulence statistics are symmetric as well. Other parameters are density, $\rho = 1$, kinematic viscosity, $\nu = 1/Re_{\tau,h}$ and channel height, $h = 1$. These values scales the friction velocity to $u_\tau = 1$.

Due to the increased drag from the roughness elements, the flow rate, i.e. bulk velocity, will be reduced, when compared to a channel with smooth walls. The bulk velocity Reynolds number, $Re_b = U_b \delta / \nu$, will therefore decrease.

4.4.1 Roughness geometry

The transverse square rods are implemented on both upper and lower walls in the computational domain. As figure 4.2 shows, the cross section is $r \times r$, and pitch-to-height ratio is $\lambda = p/r = 8$. The roughness height is $0.017h$ (0.034δ), which is just above the maximum height proposed by Jiménez [29] for the roughness to be different from bluff bodies.

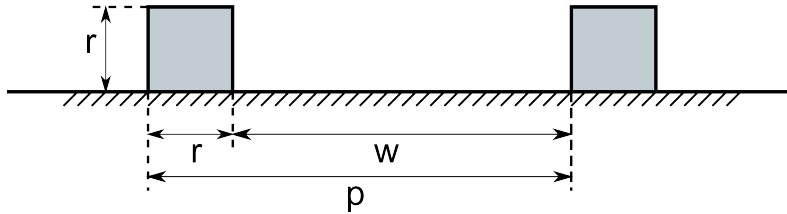


Figure 4.2: Definitions of roughness height (r), pitch (p) and roughness spacing (w) are indicated.

Non-dimensionalized, the roughness height corresponds to $r^+ = ru_\tau/\nu = 13.4$. Further, as stated in section 3.2, the equivalent sand-grain roughness height should be $k_s^+ > 70$, for the flow to be in the fully rough regime. In Ashrafiyan [4], a relation $k_s^+ \approx 5r^+$ is given, based on data from other authors. By using the the roughness Reynolds numbers (see section 3.2), k_s^+ and r^+ , a critical Reynolds number can be found:

$$Re_{\tau,h,crit} = \frac{hu_\tau}{\nu} = \frac{hr^+}{r} = \frac{hk_s^+/5}{r} = \frac{h70/5}{0.017h} = 824 \quad (4.17)$$

Based on the presented theory and proposed relations, using $Re_{\tau,h} = 790$, will cause the flow to be in the upper transitional regime.

4.4.2 Computational domain

Figure 4.3 shows a schematic overview of the orientation of the coordinate system, and the implemented square rods in the domain. The streamwise and spanwise coordinates are x and y respectively, while z denotes wall-normal direction. The lengths, (L_x, L_y, L_z) , of both the smooth- and rough channel domain are given in table 4.1. Details on the roughness elements are also included.

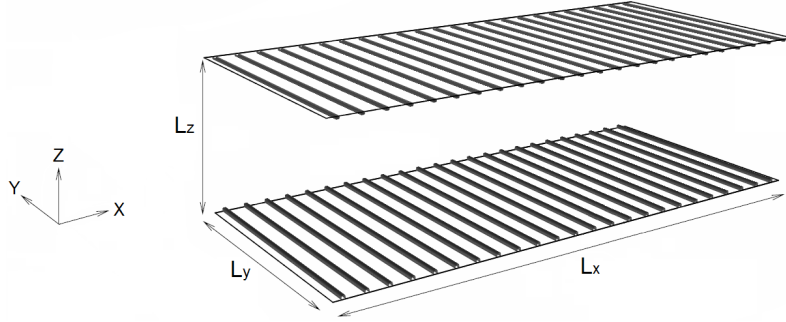


Figure 4.3: Schematic channel overview. Flow in positive x -direction. Note that this does not correspond exactly to the domain used, as the channel length, L_x , implies that only 11 spanwise ribs have to be used on each wall.

Table 4.1: Domain parameters for the smooth and rough case. Here, lengths are given in terms of channel height, h .

Case	L_x, L_y, L_z	r	p/r
Smooth	$1.5h, 0.75h, h$	-	-
Rough	$1.632h, 0.75h, h$	$0.017h$	8

4.4.3 Grid resolution

The code uses a Cartesian grid with a staggered configuration in wall-normal direction, and a collocated arrangement in streamwise and spanwise directions. In wall-normal direction, the mesh is stretched to yield a finer resolution close to the walls (i.e. non-equidistant grid), while the other two directions use a uniform grid spacing. Cell face locations in z -direction are given by:

$$z_i^f(k, s) = \frac{1}{2} \frac{\arctan(s(\frac{k}{N_z} - \frac{1}{2}))}{\arctan(\frac{1}{2}s)} + \frac{1}{2}, \quad k = 0, 1, 2, 3, \dots, N_z \quad (4.18)$$

where s is a grid stretching factor. Accordingly, cell center coordinates, z_i^c , can be found as:

$$z_i^c = \frac{1}{2}(z_i^f + z_{i-1}^f), \quad i = 1, 2, 3, \dots, N_z \quad (4.19)$$

Coordinates for the nodes inside the layer of ghost cells are also needed to provide boundary conditions. Two grid points, z_0^c and $z_{N_z+1}^c$, are added on the wall-outside at the same distance as the adjacent nodes inside the computational domain. Figure 4.4 provides an overview on the wall-normal direction indices. z_0^c and $z_{N_z+1}^c$ are the position of the ghost cell-centres.

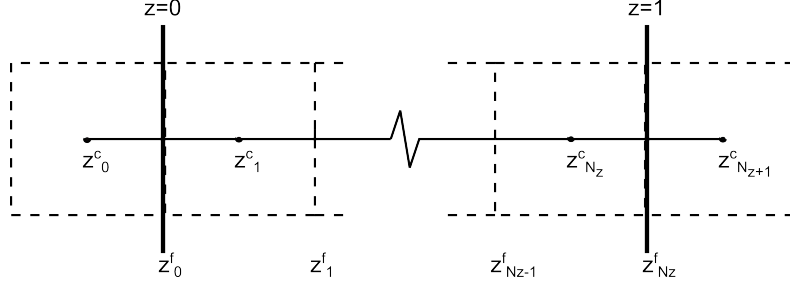


Figure 4.4: Orientation of cell faces and centres in z -direction. Bottom wall at $z = 0$, and top wall at $z = 1$.

In wall-normal direction, the cell-sizes are calculated as follows:

$$\Delta z_i = z_i^f - z_{i-1}^f, \quad i = 1, 2, 3, \dots, N_z \quad (4.20)$$

The stretch factor in equation (4.18) is set to $s = 3$, which, together with $N_z = 192$ wall-normal grid points, yields a maximum cell growth ratio of 1.0157. In wall-normalized coordinates, lengths becomes:

$$z^+ = z \frac{u_\tau}{\nu} = z \frac{u_\tau h}{\nu h} = \frac{z}{h} Re_{\tau,h} \quad (4.21)$$

A summary on cell-sizes, Δx^+ , Δy^+ and Δz^+ , and grid details is given in table 4.2. The parameters Δz_{min}^+ and Δz_{max}^+ denotes cells adjacent to the channel wall, and in the channel center respectively.

Table 4.2: Some relevant grid parameters. Domain lengths are given in terms of channel half-height, δ .

Case	L_x, L_y	N_x, N_y, N_z	Δx^+	Δy^+	Δz_{min}^+	Δz_{max}^+
Smooth	3, 1.5	48, 48, 192	11.25	5.6	0.88	2.86
Rough	3.264, 1.5	288, 48, 192	8.95	24.7	1.94	6.28

4.4.4 Boundary conditions

For the stream- and spanwise directions, periodic boundary conditions are used for all variables [24, p.29]. For the plane channel, the flow is homogeneous in these directions, which means periodic boundary conditions is preferred. This implies that the velocity field in the channel inlet is set equal to the velocity field in the

channel outlet at each timestep. Even though the streamwise homogeneity is lost in the rough channel, the roughness elements are placed periodically, so periodic boundary conditions are used also for the rough channel simulation.

For the walls, the no-slip condition is used. As figure 4.4 indicates, a layer of ghost cells outside the computational domain is used to define the boundary conditions for cell-center variables at the walls. To ensure a zero value at the wall the following is used:

$$u(z_0^c) = -u(z_1^c) , \quad u(z_{N_z+1}^c) = -u(z_{N_z}^c) \quad (4.22)$$

For the cell-face values, the wall boundary condition is simply $w(z_0^f) = 0$ and $w(z_{N_z}^f) = 0$. To ensure a zero wall-normal derivative for cell-center values, the following is used:

$$u(z_0^c) = u(z_1^c) , \quad u(z_{N_z+1}^c) = u(z_{N_z}^c) \quad (4.23)$$

To implement the square rods, velocities are set to zero inside the roughness geometry. The number of grid points, and domain length in streamwise direction is chosen so the sides of the roughness elements coincides with the grid. In this way, the no-slip condition is enforced exactly at the roughness surface, as the surface of the roughness elements follows the cell-center points, shown in figure 4.5. In wall-normal direction, however, due to the grid stretching prescribed by equation (4.18), the cell-center points does not necessarily coincide perfectly with the given roughness height. The cell center points closest to the specified roughness height is therefore chosen as the top surface.

Using the grid parameters given in table 4.2, the roughness element is resolved using 3 grid points in streamwise direction, and 6 grid points in wall-normal direction. For comparison, Ashrafiyan [4] used 4 and 8 grid points in these directions respectively.

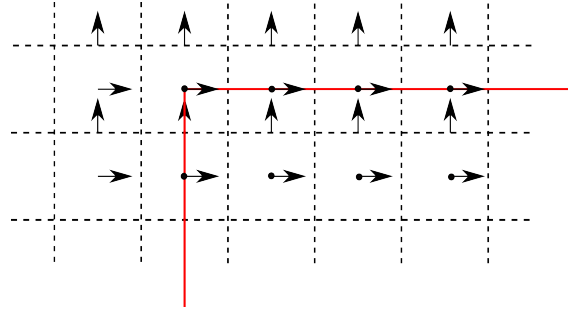


Figure 4.5: Schematic sketch of the top of one roughness element. The dots are the cell-center pressure points, the dashed lines are the grid cells, and the solid, red line is the roughness element surface. The arrows represents streamwise and wall-normal velocity vectors.

4.4.5 Turbulence initial condition

The initial condition for the velocities and pressure can either be set as a random velocity field, or a fully developed turbulent velocity field from a previous simu-

lation. For the smooth channel simulation, a fully developed flow field from an earlier simulation was used, but for the rough channel however, no flow data, either from DNS or LES was available, so the simulation started from a random set of disturbances.

4.4.6 Computation and parallelization

The FORTRAN code is fully parallelized, which means that the domain is split into multiple sections in wall normal direction¹², so multiple processors can be used simultaneously. The top and bottom grid point variables must then be communicated to the adjacent slices using MPI. Computational time was available from the High Performance Computing (HPC) centre at NTNU, using the Vilje supercomputer.

4.4.7 Time sampling and statistics

For the smooth, and relatively small channel simulation, a fully developed flow field from an earlier simulation was used as initial condition. Thus, samples could be included to form statistical data from the very first calculated time steps. The simulation was run using a timestep of $\Delta t = 10^{-4}$ on 16 processors. This is the same as used by Gillissen [24] ($\Delta t = 3.6 \times 10^{-2} \nu/u_\tau^2$). The maximum allowed Δt was reported to be $\Delta t_{max} = 1.7 \times 10^{-4}$, which implies that the time step used was appropriate. From the already fully turbulent flow field, about 3 hours was needed to get 300 samples in time. Here, the velocity field was stored for each 1000 time steps, and the computational time was about 0.045 s for each time step.

The rough-wall simulation was first advanced forward, using 32 processors, from the initial set of random disturbances, until a realistic turbulent flow field had developed. This, in general, requires a smaller time step in the beginning, so $\Delta t = 10^{-5}$ was used. In this state, maximum allowed Δt from the CFL-criterion, equation (4.15), was reported to be $\Delta t_{max} = 7.3 \times 10^{-5}$. The simulation was run for 12 hours, and the bulk velocity was used as an indicator to check whether a statistically steady state was reached. During this time, the bulk velocity was reduced from $U_b^+ \approx 15$ to $U_b^+ \approx 11$. Now, time step was set to $\Delta t = 2 \times 10^{-5}$, and the simulation was advanced forward another 120 hours. The velocity field was stored each 5000 time steps, and 400 samples in time was obtained. In this statistically steady state, the computational time was about 0.15 s per time step, and the maximum allowed Δt was reported to be $\Delta t_{max} = 8.8 \times 10^{-5}$.

¹²To solve the Fourier transformed Poisson equation, the domain is split in streamwise direction as well [24, p.31].

5 Smooth channel results

The following chapter presents the results from the smooth channel simulation. To save computational cost, a relatively small domain is chosen. Despite being very short in streamwise and spanwise directions, this is the same domain size as used by Gillissen [24] and Jiménez & Pinelli [30]. The results are compared with the DNS-results from Kim et al. [32] at $Re_\tau = 180$ ($Re_b = 2800$). Their data is thoroughly verified and has been used as a solid reference over the years. Note that the domain used in the present case is roughly 18 times smaller than in the case of Kim et al. [32].

The domain size and grid resolution is summarized and compared in table 5.1. As can be seen, the resolutions are almost identical, perhaps apart from the wall-normal direction, where a relatively cautious grid stretching is used in the present case. The grid point resolution results in a total number of 442 368 grid points in the present simulation, compared to 3 962 880 points in the case of Kim et al. [32].

Table 5.1: Relevant parameters for the smooth channel. Domain size is given in terms of channel half-height, δ .

Case	L_x, L_y	N_x, N_y, N_z	Δx^+	Δy^+	Δz_{min}^+	Δz_{max}^+
Smooth	3, 1.5	48, 48, 192	11.25	5.6	0.88	2.86
Kim et al. [32]	$4\pi, 2\pi$	192, 160, 129	12	7	0.1	4.4

The data is averaged in the homogeneous directions after reaching a statistically steady velocity field. In this statistically steady state, the simulation is run long enough in time so that averaging is performed over a total number of 300 samples. Since all flow statistics are symmetric, only one half of the channel is presented here.

5.1 Mean velocity profiles

Figure 5.1 shows the mean velocity profile over the channel half-height. The mean bulk velocity, defined in equation (5.1), over the time sampling interval is equal to $U_b^+ = 15.624$, which corresponds to a bulk Reynolds number of $Re_b = 2812$. This is essentially the same as $U_b^+ = 15.63$ in Kim et al. [32].

$$U_b^+ = \frac{1}{h} \int_0^h u^+ dz \quad (5.1)$$

Here, u^+ is the normalized mean velocity, defined from equation (3.2). The profile corresponds well with the data from [32], but a slightly underestimate can be observed from $z/\delta = 0.3$ and outwards. The channel centreline velocity is $u_{CL}^+ = 18.17$, compared to $u_{CL}^+ = 18.20$ in [32], which is only 0.16% less.

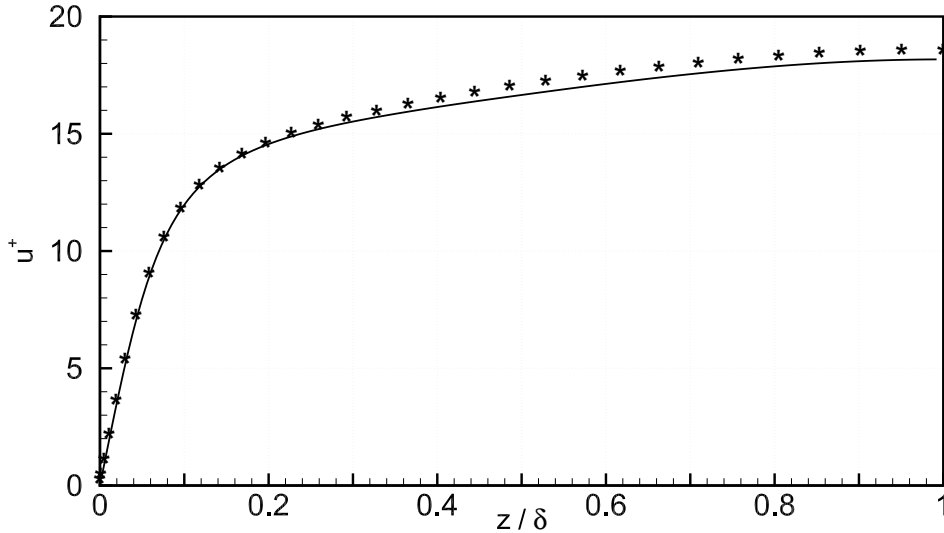


Figure 5.1: Mean velocity in global coordinates, compared to data from Kim et al. [32] (*).

Looking at figure 5.2, the velocity profile is compared to the law of the wall, which describes the velocity in the viscous sublayer and logarithmic layer according to equation (5.2).

$$u^+ = \begin{cases} z^+ & \text{for } z^+ < 5 \\ \frac{1}{\kappa} \ln z^+ + A & \text{for } z^+ > 30 \end{cases} \quad (5.2)$$

The constants are the same as given in section 3.3, $\kappa = 0.41$ and $A = 5.5$. The profile is in good agreement with the law, and smoothly connects the viscous sublayer to the logarithmic layer in the region $5 < z^+ < 30$.

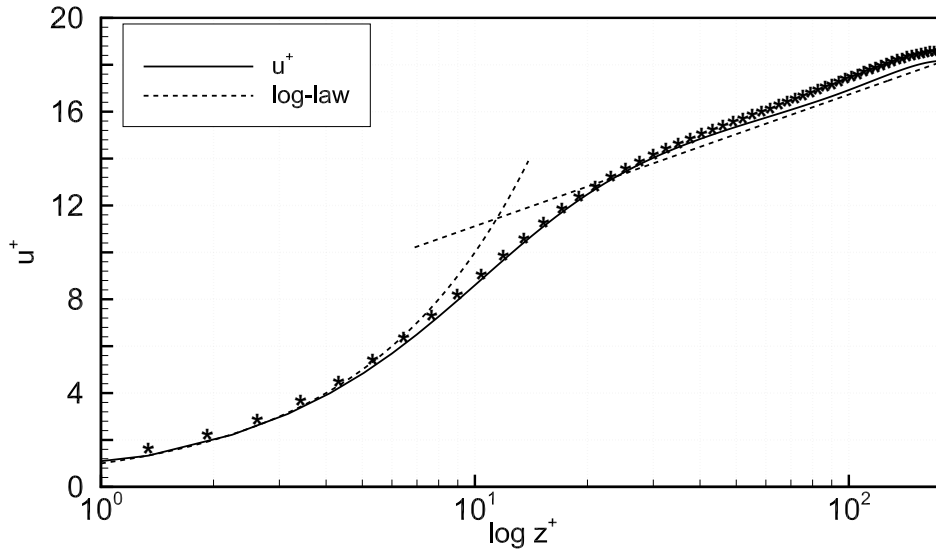


Figure 5.2: Mean velocity in wall coordinates compared to data from Kim et al. [32] (*), and the law of the wall.

5.2 Turbulence intensities

Figure 5.3 shows the root mean square (r.m.s.) of the velocity fluctuations in all three coordinate directions across the channel half-height. Here, the r.m.s. is defined as follows:

$$u_{i,rms}^+ = \frac{\sqrt{u_i'^2}}{u_\tau} \quad (5.3)$$

Clearly, it can be seen that the results deviates from the data of Kim et al. [32] in magnitude, while the shapes are in good agreement. The streamwise profile is overestimated near the wall, while the spanwise and wall-normal profiles are underestimated. The peak in u_{rms}^+ is about 4% higher than in [32]. It is also interesting to compare with Gillissen [24, fig.5.1,p.49], who used the same channel dimensions as in the present simulation. In his data, the streamwise profile peaks at about $u_{rms}^+ = 3$, but collapses with the Kim et al. [32] data at $z^+ = 70$ and outwards. This is relatively consistent with the present results. Further, the spanwise and wall-normal profiles has a lower magnitude than the Kim et al. [32]-data throughout the channel height. This is in agreement with the data of Gillissen [24] for $z^+ < 50$, but from here and outwards, his profiles for v_{rms}^+ and w_{rms}^+ has a slightly larger magnitude compared to Kim et al. [32].

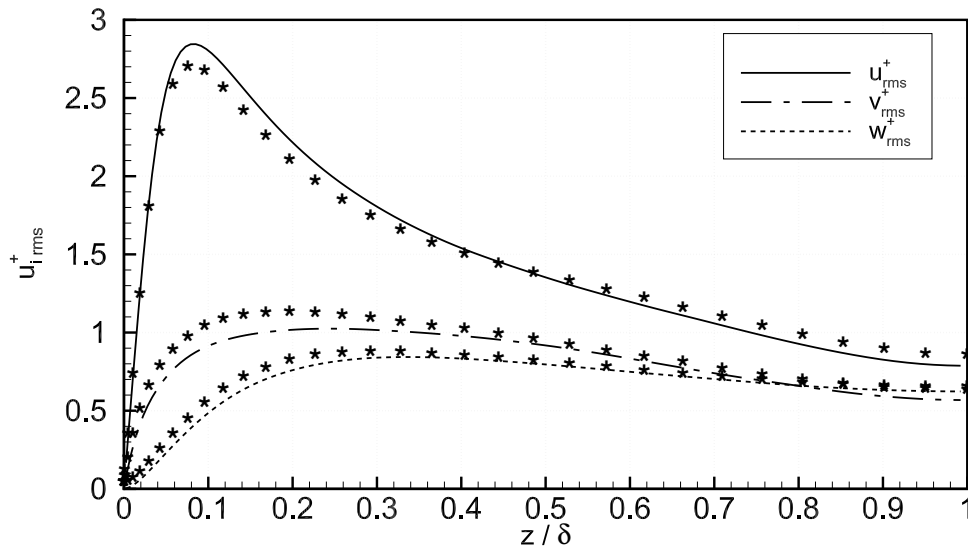


Figure 5.3: R.m.s. of velocity fluctuations in global coordinates, and data from Kim et al. [32] (*).

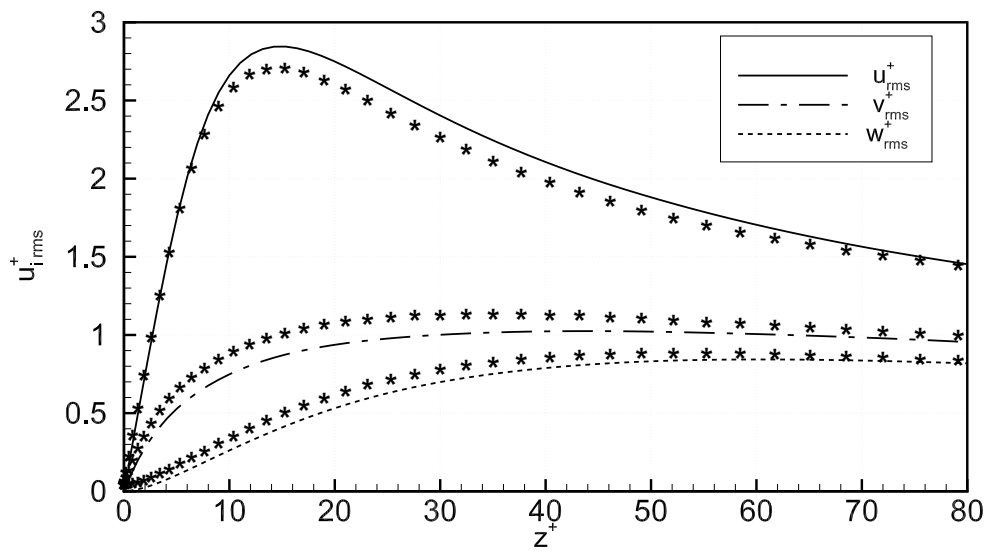


Figure 5.4: R.m.s. of the velocity fluctuations in wall coordinates, and data from Kim et al. [32] (*).

5.3 Reynolds shear stress

For a plain channel flow, the mean wall-normal velocity is zero, $\bar{w} = 0$, and due to homogeneity, streamwise derivatives are also zero, $\partial/\partial x = 0$. From the averaged Navier-Stokes equation, equation (2.8), what is left of the stress term is:

$$\tau_{total} = \nu \frac{d\bar{u}}{dz} - \overline{u'w'} \quad (5.4)$$

The two terms are plotted in figure 5.5 across the channel half-height. The $-\overline{u'w'}$ profile does not show noticeable deviation from the Kim et al. [32] data, and follows a straight line through the channel center. For the viscous stress, some discrepancy can be seen from $z^+ = 30$ and outwards. Even though deviation can also be seen for the mean velocity profile, figure 5.2, the viscous stress is only dependent on the shape of $u^+(z)$, thus the deviation indicates that the shapes of the mean velocity profile are somewhat different.

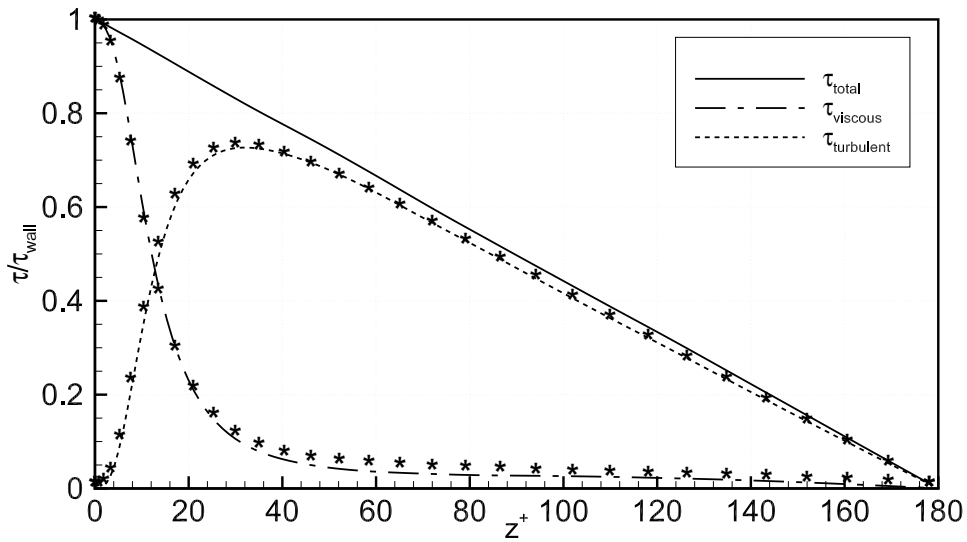


Figure 5.5: Viscous and turbulent shear stress across the channel half-height. Data from Kim et al. [32] (*).

5.4 Vorticity

The r.m.s. of the vorticity fluctuations are shown in global and wall coordinates in figure 5.6 and figure 5.7 respectively. $\omega_{i,rms}^+$ is defined according to equation (5.5):

$$\omega_{i,rms}^+ = \sqrt{\overline{\omega'^2}} \frac{\nu}{u_\tau^2} \quad (5.5)$$

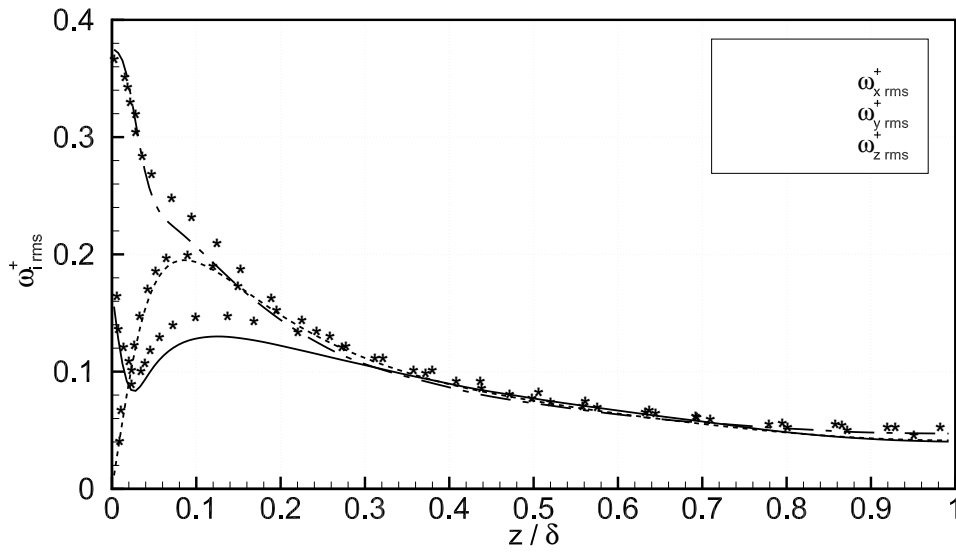


Figure 5.6: R.m.s. of the vorticity fluctuations in global coordinates, compared to data from Kim et al. [32] (*).

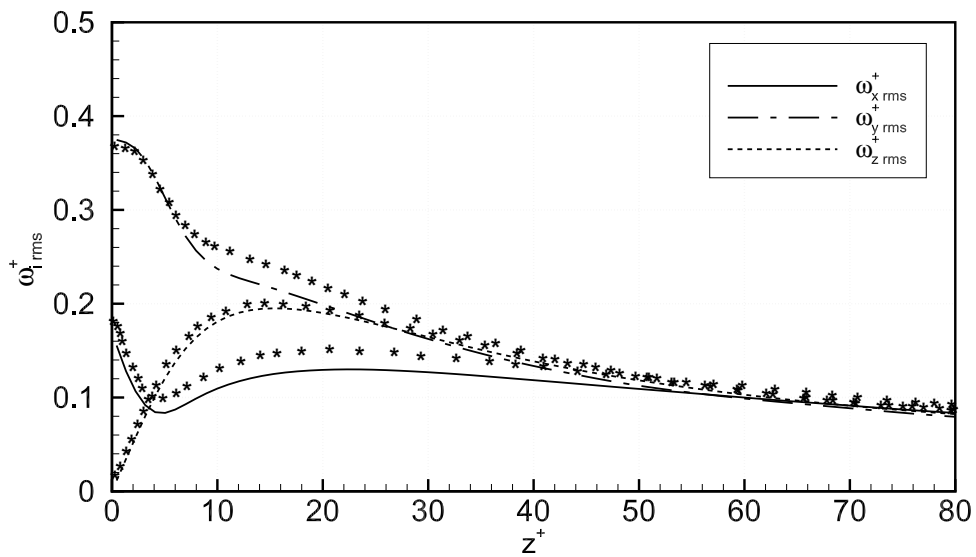


Figure 5.7: R.m.s. of the vorticity fluctuations in wall coordinates, compared to data from Kim et al. [32] (*).

Mathematically, the vorticity, ω , is defined as the curl of the velocity field, and represents the rotation of fluid particles. Vorticity is always present in turbulence, both in the structures of the large energy carrying scales, and the small dissipative scales.

As can be seen from the figures, the three components are highly anisotropic near the walls, while in the outer region, they are more or less identical. The streamwise vorticity has a its maximum value at the wall, then a local minima and maxima at $z^+ \approx 5$ and $z^+ \approx 20$ respectively, the same as in the data of Kim et al. [32]. The magnitude of the peak values are however 20% less. The wall-normal vorticity, $\omega_{z,rms}^+$, goes to zero at the wall, and the profile almost overlaps the data from [32] throughout the channel. The spanwise vorticity, $\omega_{y,rms}^+$, also overlaps the data from Kim et al. [32], but only out to $z^+ \approx 8$. From here, a relatively large discrepancy can be observed all the way to $z^+ \approx 50$.

6 Rough channel results

This chapter presents the results from the rough channel simulation together with relevant data for comparison. A Reynolds number of $Re_\tau = 395$ is used, which is in the range of which many researchers have performed DNS of both smooth and rough channel flow. The smooth channel comparison is the mid- Re case of Moser et al. [41], $Re_\tau = 395$, and the rough channel comparison is of Ashrafian [4], $Re_\tau = 400$. Other relevant comparisons are the square-rib roughness simulation of Narasimhamurthy & Andersson [42], $Re_\tau = 400$, and Leonardi et al. [39], $Re_\tau = 180$. The two latter cases, however, use much larger roughness elements.

Relevant domain and grid details for the different cases are compared in table 6.1. As can be seen, the streamwise and spanwise domain length in the present simulation is about half the lengths of Moser et al. [41] and Ashrafian [4]. The number of grid points is also reduced, except for the wall-normal direction, to save computational cost. The total number of grid points is 2 654 208, compared to 19 660 800 and 9 486 336 for the rough and smooth channel comparisons respectively. Compared to the rough channel of Ashrafian [4], the domain size is about four times smaller, and number of grid points is about seven times less. Looking at the grid resolution, however, the wall-normal grid spacing is comparable, while the spanwise grid resolution is about three times than what is used in the other two cases. Also, comparing the streamwise resolution for the rough channels, the spacing in the present simulation is about three times larger.

Table 6.1: Parameters for some relevant cases. The smooth channel case of Moser et al. [41] is for the Reynolds number $Re_\tau = 395$. Channel lengths given in terms of channel half-height δ .

Case	Re_τ	Re_b	L_x, L_y	N_x, N_y, N_z	Δx^+	Δy^+	Δz_{min}^+	Δz_{max}^+
Present	395	4070	3.264, 1.5	288, 48, 192	8.95	24.7	1.94	6.28
Ashrafian [4]	400	4200	6.528, π	768, 160, 160	3.4	7.85	1.7	15.6
Moser et al. [41]	395	6900	$2\pi, \pi$	256, 192, 193	10.0	6.5	-	6.5

Figure 6.1 shows the instantaneous and averaged contour plots of the streamwise velocity, u^+ . The mean velocity field is averaged, first in spanwise direction, then over 400 samples in time. After averaging in time, a periodicity equal to the pitch

length, p , can be observed. Thus, to obtain better statistics, we take advantage of this streamwise quasi-homogeneity by averaging unit-wise at two characteristic locations. One is at the roughness element center-point (mid crest), and one in the center between two roughness elements (mid cavity). These locations are indicated in figure 6.6b, at $x/p = 1.0$ and $x/p = 0.5$ respectively. For the domain used, this corresponds to a total of 11 unit-wise samples for each location. Further, averaging is performed over both sides of the channel, benefiting from the channel symmetry. This is with the exception of some figures, included to show the symmetry of the solution over the full channel height. From figure 6.1, it can be seen that the roughness elements are very small compared to the channel height, and for both cases the flow pattern in the very near wall region is quite similar, and shows a periodicity also for the instantaneous flow field.

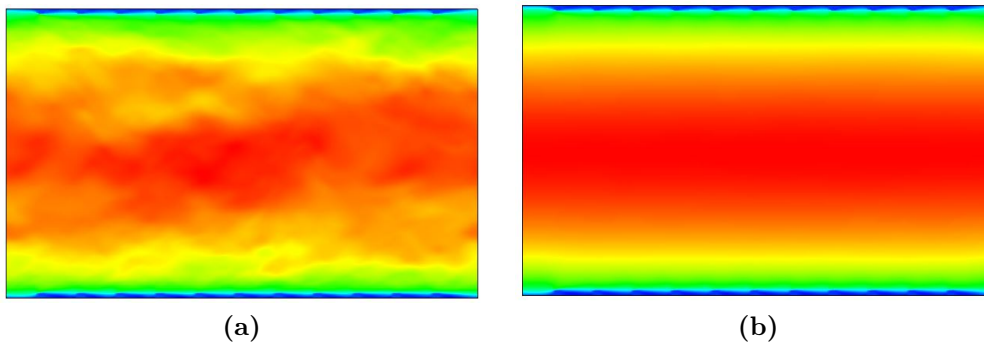


Figure 6.1: Instantaneous and averaged contour plot of stream-wise velocity, u^+ .

Figure 6.2 shows the evolution of the bulk velocity, U_b^+ , in time, i.e. the flow development from the initial random disturbances to a statistically steady turbulent state. The bulk velocity is defined from equation (5.1). The largest decrease in bulk velocity at the beginning of the simulation, where the bulk velocity decreased from $U_b^+ \approx 15$ to $U_b^+ \approx 11$, is not shown in this plot. Samples are averaged in the interval between $t = 20$ to $t = 60$. For details regarding time steps and data collection, see section 4.4.7.

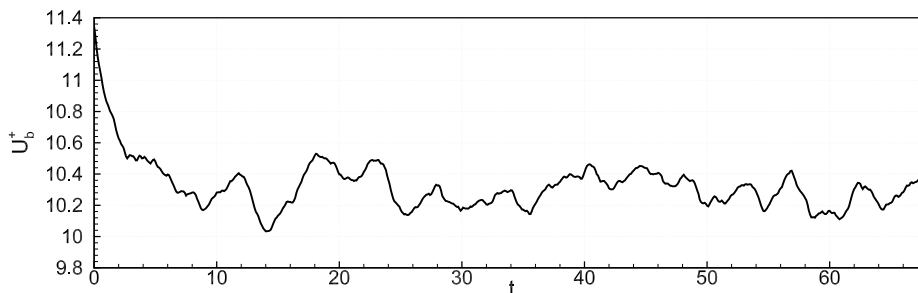


Figure 6.2: Evolution of the bulk velocity, U_b^+ , in time.

6.1 Mean velocity profiles

Figure 6.3 shows the mean velocity profile normalized with the channel centerline velocity. u^+ is defined from equation (3.2). The centerline mean velocity is $u_{CL}^+ = 12.83$, and bulk velocity is $U_b^+ = 10.307$ (at both streamwise locations), which results in a bulk Reynolds number of $Re_b = U_b^+ \delta / \nu = 4070$. This corresponds to a decrease of $\approx 40\%$ compared to the smooth channel of Moser et al. [41]. For comparison, the centerline mean velocity is $u_{CL}^+ = 20.13$ and bulk velocity $U_b^+ = 17.54$ in Moser et al. [41]. The velocity profile shows a clear deviation from the smooth channel profile due to the increased drag. Compared to the rough channel of Ashrafian [4], the mid-crest velocity profile almost overlaps in the near-wall regions, but it can be seen that the profile in the present simulation is not perfectly symmetric, as the profile from Ashrafian [4] is.

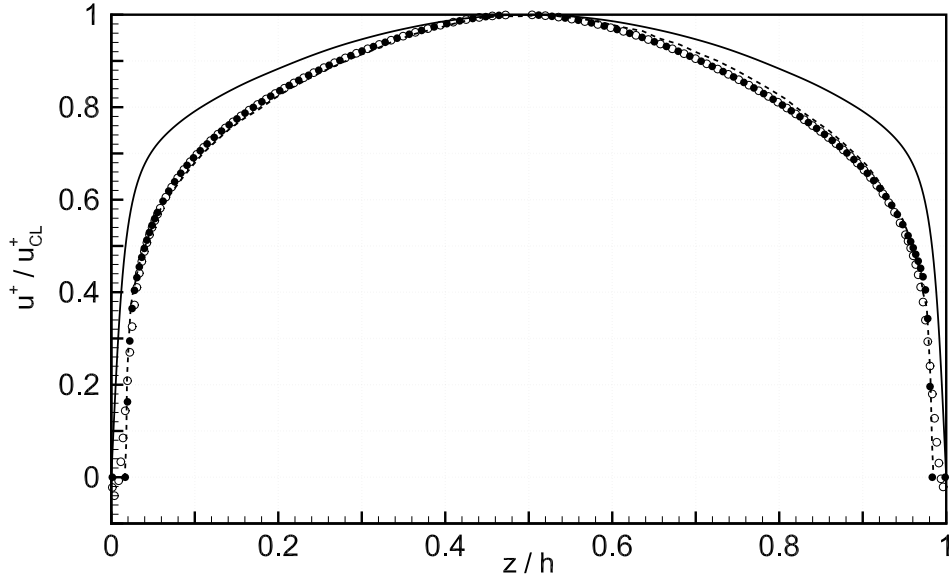


Figure 6.3: Mean streamwise velocity normalized by the channel centerline velocity in global coordinates. Symbols are rough channel data, at mid crest, $x/p = 0.0$ (\bullet) and mid cavity, $x/p = 0.5$ (\circ). Solid line is smooth channel data from Moser et al. [41], and dashed line is mid crest data from Ashrafian & Andersson [5].

Figure 6.4 shows the velocity profile in wall coordinates. The vertical shift in the velocity profile is clearly shown. Going back to equation (3.5), and rewriting, the modified law of the wall can be given as:

$$u^+ = \frac{1}{\kappa} \ln(z^+) + A - \Delta u^+ \quad (6.1)$$

where the constants κ and A are the same as given in section 3.3, $\kappa = 0.41$ and $A = 5.5$, and the downward shift, Δu^+ , is ≈ 7.1 . This is the same as reported by Ashrafian [4]. From equation (3.7), an equivalent sand-grain roughness can be found

from the observed Δu^+ , corresponding to $k_s^+ = 63$, which is in fact in the upper transitional regime. Further, both mid crest and mid cavity data from Ashrafian [4] are compared to the present simulation, and the profiles are in good agreement, almost overlapping in both the inner and outer region.

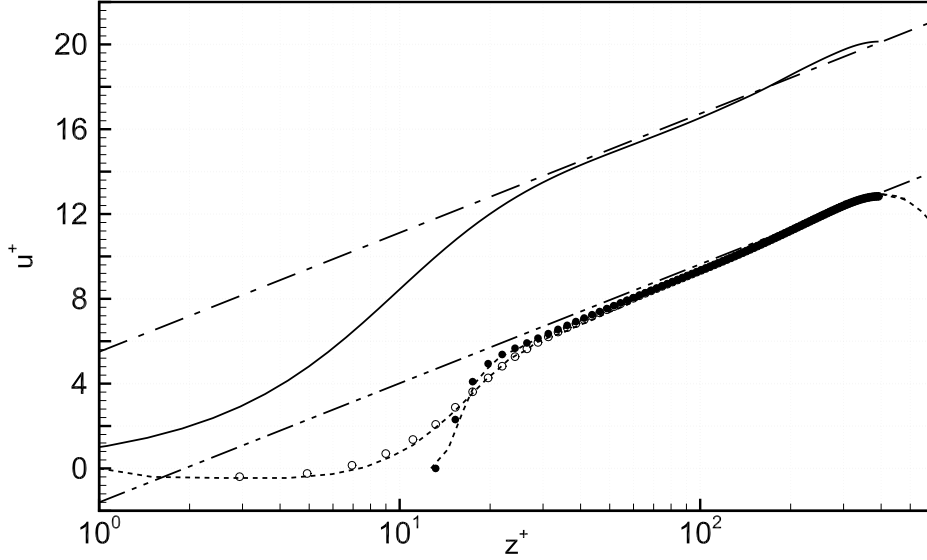


Figure 6.4: Mean streamwise velocity in wall coordinates. Legend as in figure 6.3, except that here, dashed lines represents both mid crest and mid cavity data from Ashrafian & Andersson [5]. Dash-dot line are the log-law, equation (3.3), and dash-dot-dot line are the modified log-law for roughness, equation (6.1), with $\Delta u^+ = 7.1$.

Further, from figure 6.4, it can be seen that the mid crest and mid cavity data overlaps outside $z^+ \approx 60$. This indicates that the velocity profile is unaware of the surface details outside the roughness sublayer, $z^+ \approx 5r^+$, as the profile is independent of streamwise position in this outer layer. It is also shown that the logarithmic profile is maintained in this region. This is in agreement with the wall similarity hypothesis.

The spanwise and wall-normal mean velocities, defined as $v^+ = \bar{v}/u_\tau$ and $w^+ = \bar{w}/u_\tau$ respectively, are shown in figure 6.5. For a smooth channel, both velocities should essentially be zero across the channel height, and for the spanwise velocity this should also be the case for the rough channel. As the figure shows, this is clearly not the case. Integrated over the channel height, v^+ results in a spanwise bulk velocity of $V_b^+ = 0.0152$, which is 0.14% of U_b^+ . The peaks of the spanwise velocity have a magnitude of ± 0.04 , which corresponds to 0.3% of the streamwise maximum velocity, u_{CL}^+ . The spanwise domain length, L_y , poor grid resolution, N_y , and the time sampling are three different factors that can possibly lead to this behaviour. Thus, the mean spanwise velocity can be seen as an indicator of the quality of the above mentioned parameters. The wall-normal velocity, however, is in good agreement with what is indicated in Ashrafian et al. [7, fig.4a]. In the

mid-cavity section, there is maximum negative velocity at the same height as the roughness element, and mid crest, the maximum velocity is found to be $r/2$ away from the top surface. Towards the channel center section, the velocity decreases to zero, as it should.

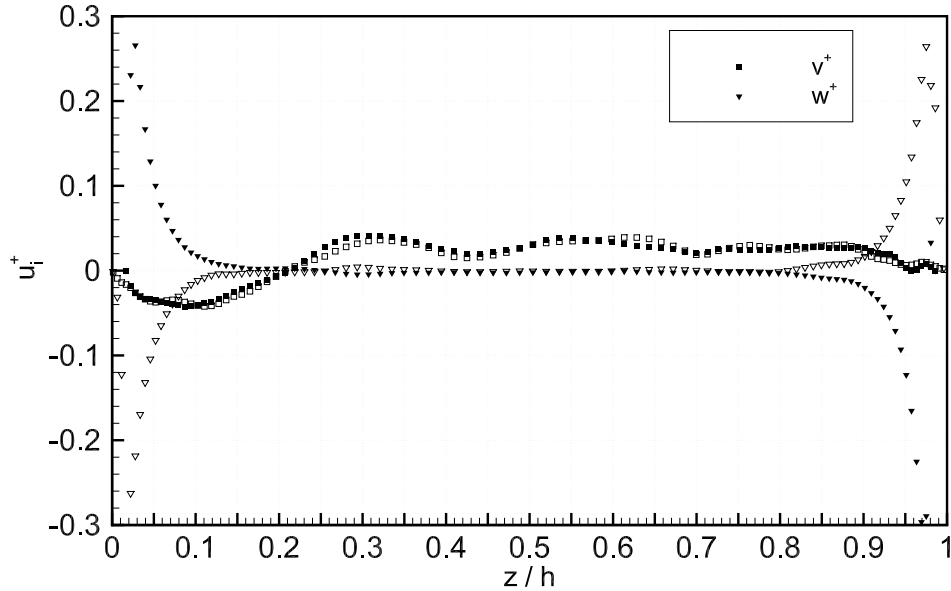


Figure 6.5: Mean spanwise and wall-normal velocities in global coordinates. Filled symbols ($\blacksquare, \blacktriangledown$) are mid crest data, while open symbols are mid cavity (\square, \triangledown) data.

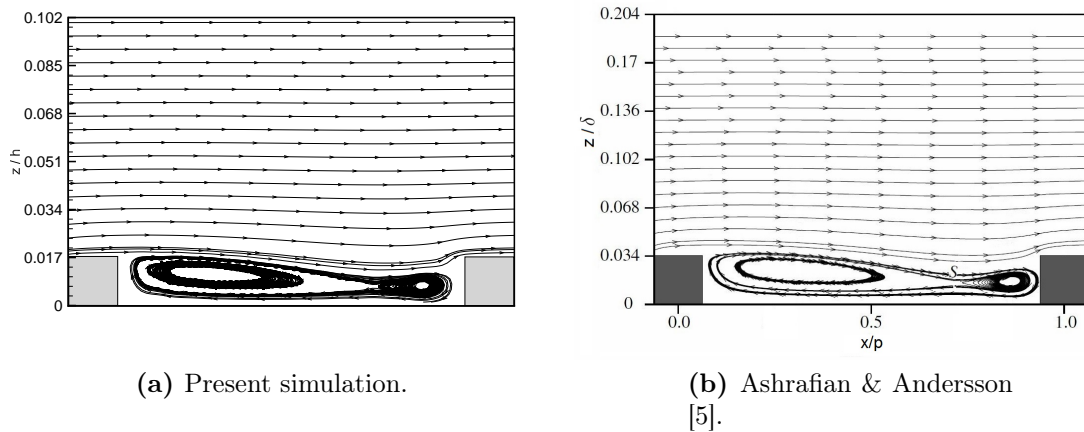


Figure 6.6: Streamlines between two roughness elements. Comparison between present simulation, and figure from Ashrafiyan & Andersson [5, fig.5].

Figure 6.6a shows the streamlines, based on u^+ and w^+ , between two roughness elements. As can be seen, the flow never reattaches to the wall, as it was indicated

for k -type roughness in section 3.4. A large separation bubble that consists of two vortexes of equal sign, fills each cavity. Comparing the flow with the results from Ashrafian [4], shows an almost identical flow pattern, with the center of the vortexes being almost at the same locations. The saddle point is indicated in figure 6.6b. It seems that the streamlines become parallel around $z/h = 0.05$, but figure 6.5 suggests that this is not the case entirely until $z/h = 0.15$ is reached. Compared to Leonardi et al. [39, fig.2], who used the same height-to-pitch ratio, the pattern is relatively different. They observed that the flow reattached to the surface about $4.8r$ behind the square rod. However, their rods were much bigger; $r^+ = 90$, compared to $r^+ = 13.4$ in the present case.

6.2 Turbulence intensities

The turbulence intensity in streamwise direction, $I = u_{rms}^+ / u^+$, is shown in figure 6.7. The root mean square of the velocity fluctuations is defined from equation (5.3). Compared to the smooth channel data, the roughness generates much higher turbulence levels, particularly in the near wall region, but the turbulence level is also higher throughout the channel height. The results are also in good agreement with Ashrafian [4], as the profiles collapse both for the mid crest and mid cavity region.

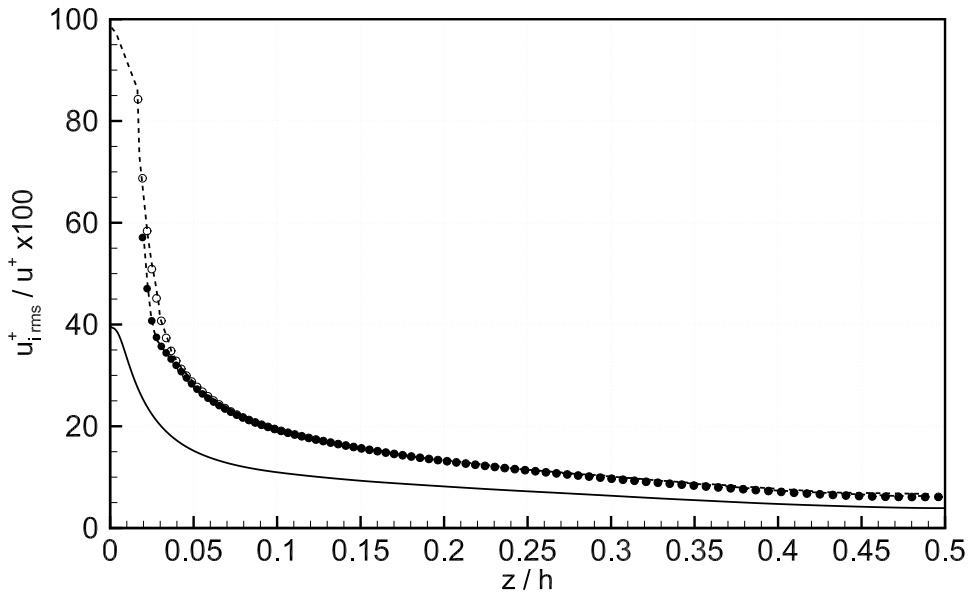


Figure 6.7: Turbulence intensity across the channel half-height. Mid crest (\bullet) and mid cavity (\circ) data. Solid line is smooth channel data from Moser et al. [41], while dashed lines are rough channel data from Ashrafian [4].

The r.m.s. of the velocity fluctuations are shown across the full channel height in figure 6.8 for all three directions. The largest variations are found in the region

very near the roughness elements, while the profiles more or less collapses with the smooth channel data in the outer region. This figure also shows that the second order statistics are not fully symmetric at both sides of the channel. At the bottom wall ($0 < z/h < 0.5$) the streamwise and wall-normal profiles are somewhat smaller in magnitude compared to the top wall ($0.5 < z/h < 1$), while the spanwise profile seems to oscillate around the smooth channel data, showing a relatively large deviation at the channel center. Thus, the results will benefit from averaging over the two sides. The peaks are, however, relatively symmetric, except for the wall normal profile, which has a peak that collapses with the smooth channel data in the top half of the channel, while being slightly less at bottom half.

Figure 6.9 are given in wall coordinates, with each gridline corresponding to the height of the roughness element. Note that all following results are averaged over both sides of the channel. As can be seen, the mid cavity and mid crest profiles collapses between $z^+ = 3r^+$ and $z^+ = 4r^+$ for all components. The peak in mid cavity streamwise fluctuation is reduced by approximately 17% compared to smooth channel data, while the mid crest fluctuations has a much flatter profile, with a smaller peak that is shifted one roughness height outwards relative to the mid cavity peak. For the spanwise mid crest fluctuation, a sharp peak, can be observed. As stated in Ashrafian & Andersson [5] and Ikeda & Durbin [28], the spanwise fluctuation is intensified, due to the blocking of the streamwise fluctuation. The wall-normal fluctuations are most unaffected by the presence of roughness, and the profiles have a very similar shape to that of the smooth channel.

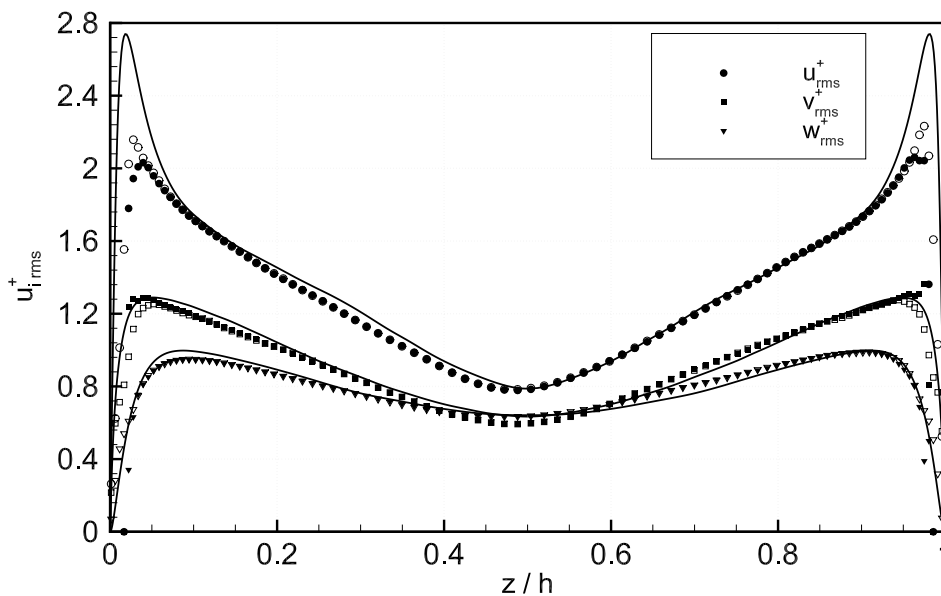


Figure 6.8: R.m.s. of velocity fluctuations in global coordinates. Filled symbols ($\bullet, \blacksquare, \blacktriangledown$) are mid crest data, while open symbols are mid cavity (\circ, \square, ∇) data. Solid lines are smooth channel data from Moser et al. [41].

As mentioned in section 3.5, the results indicates, that for the fluctuations, the

effect of roughness is most pronounced in the roughness sublayer, stretching out to a distance between 3 to 5 roughness heights. This corresponds to $z/h = 0.051-0.085$ or $z^+ = 40.2 - 67$ in wall units. The data of Ashrafian [4] is given for comparison in figure 6.10, and here, the profiles overlaps almost perfectly with the smooth channel data outside $z^+ = 5r^+$. For the present results, this is the case as well. However, small discrepancies can be observed for the spanwise profiles. Comparing the present results to that of Ashrafian [4], figure 6.9 and 6.10, the exact same trends in all profiles can be seen, and the results are in general in very good agreement.

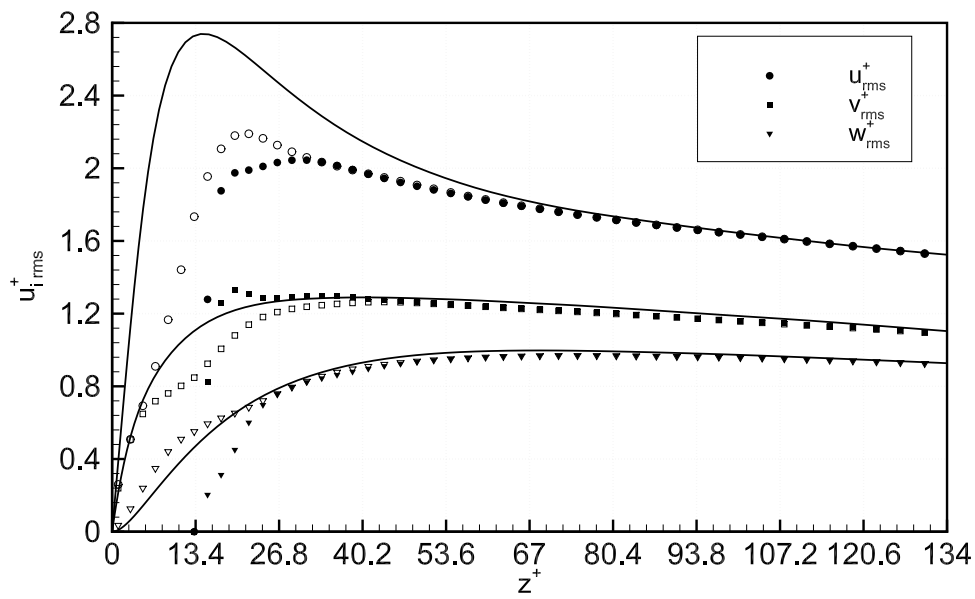


Figure 6.9: R.m.s. of velocity fluctuations in global coordinates. Legend as in figure 6.8.

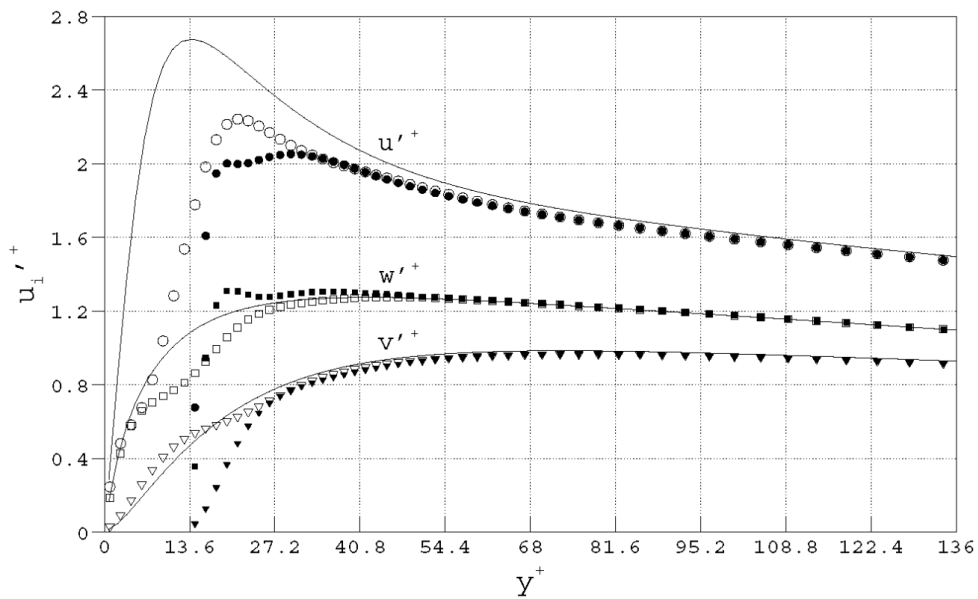


Figure 6.10: Figure from Ashrafian & Andersson [5] for comparison. R.m.s. of velocity fluctuations in global coordinates. Solid lines are from a smooth channel DNS at $Re_\tau = 400$ [5]. Note that the coordinate system is different, as the spanwise and wall-normal direction is interchanged compared to the present simulation.

6.3 Reynolds stresses

The following section presents the three Reynolds normal stresses, as well as the Reynolds shear stress, in global coordinates. The terms are normalized with u_τ^2 , that is: $\overline{u'_i u'_i}^+ = \overline{u'_i u'_i} / u_\tau^2$. The cross-channel symmetry of the normal stresses is indicated in figure 6.8, as the stresses, essentially, are equal to $u_{i,rms}^{+2}$.

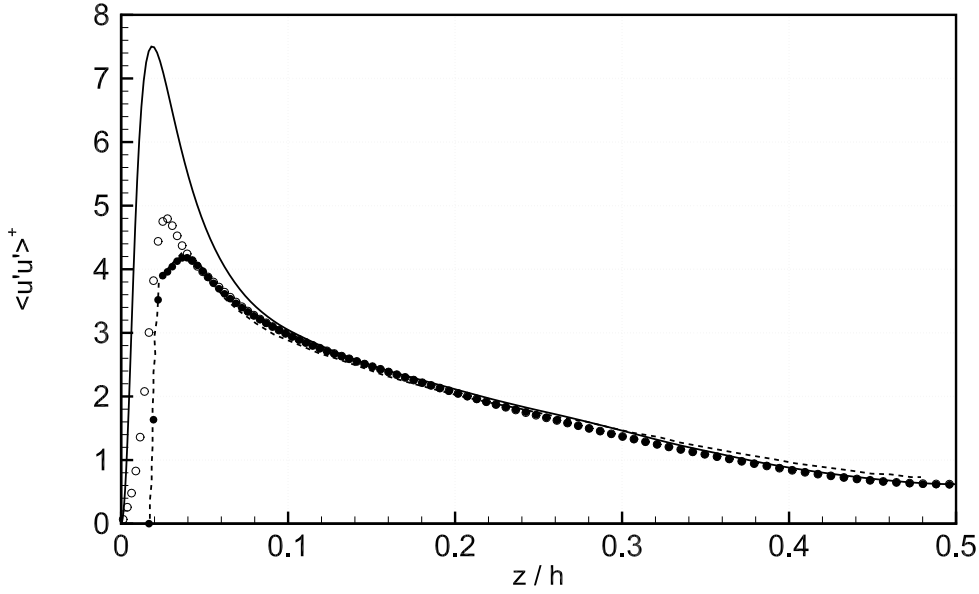


Figure 6.11: Streamwise normal stress, $\overline{u'u'}$ in global coordinates. Mid crest (\bullet) and mid cavity (\circ) data. Solid line is smooth channel data from Moser et al. [41], and dashed line is mid crest data from Ashrafian & Andersson [5].

The streamwise stress is shown in figure 6.11. It can be seen that the peak value is severely decreased by the introduction of roughness. Krogstad et al. [34] states that this is due to the breakup of the streamwise vortices. The roughness effect is, however, only felt very close to the wall, as the mid crest and mid cavity profiles collapses at $z^+ = 3r^+$. Compared to the mid crest data of Ashrafian [4], the results are in very good agreement, as the profiles overlaps perfectly.

The spanwise mid crest stress profile is characterized by two distinct peaks in the vicinity of the roughness element, which is the exact same trend as in [4]. The first peak has a slightly higher magnitude, while the second is almost identical. The profiles at the streamwise locations collapses at $z^+ = 4r^+$. Compared to the smooth channel data (as well as the rough channel data), the magnitude of $\overline{v'v'}$ is slightly less in the region $0.05 < z/h < 0.2$ and in the channel center.

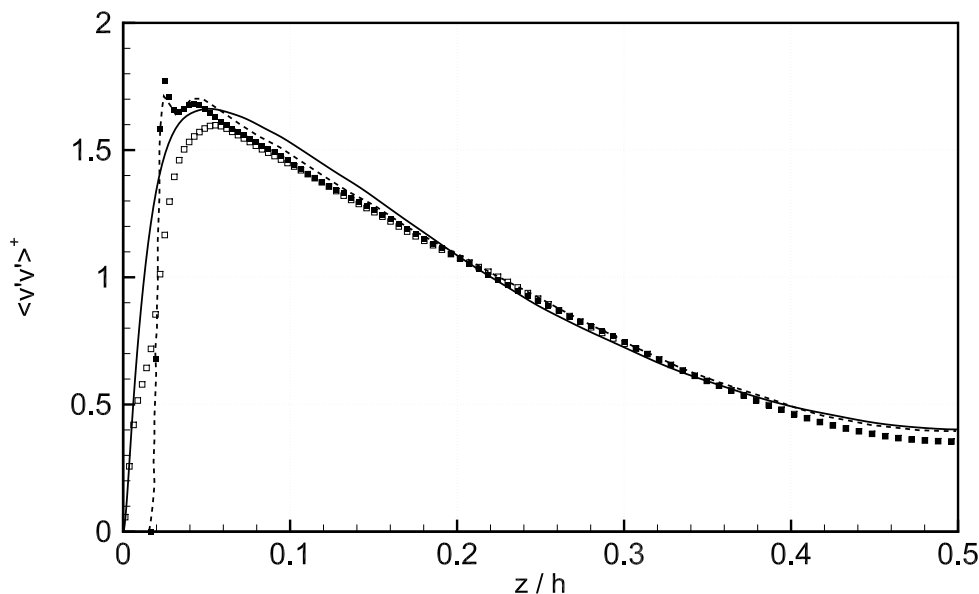


Figure 6.12: Spanwise normal stress, $\overline{v'v'}$ in global coordinates. Mid crest (■) and mid cavity (□) data. Line legend as in figure 6.11.

For the wall-normal direction, Krogstad & Antonia [35] suggested that rib roughness will have a strong effect on $\overline{w'w'}$, and showed that this stress was most affected by the roughness in both the inner and outer layer. This was for boundary layer flow, however, and is not found in the present case. Here, the roughness effect is very small, as the profiles for the two streamwise locations collapses already at $z^+ = 2r^+$. In magnitude, the peak at $z/h = 0.09$ is reduced by approximately 10% compared to the smooth channel data, and matches the rough channel data perfectly. For all the plots, it is observed that only the streamwise stress follows the smooth channel profile smoothly, as both the spanwise and wall-normal stress profiles crosses the smooth channel profiles at approximately $z/h = 0.2$ and $z/h = 0.4$.

Figure 6.14 shows the shear stress, $-\overline{u'w'}$. The mid crest and mid cavity profiles collapses at ≈ 0.07 , or $z^+ \approx 4r^+$ in wall coordinates, and forms a straight line, as expected. The small discrepancies that can be observed between the two locations are likely to be related to the statistical averaging. The rough wall profiles from Ashrafian [4] collapses at $z^+ = 5r^+$ [5, fig.13], and more or less overlaps the smooth channel data from Moser et al. [41]. The peak in the mid crest profile matches the data of [4] exactly. The mid cavity profile is also in good agreement with [4] (comparison not shown here), having to local near-wall maxima at $z^+ = 20$ and $z^+ = 40$. The inner maxima is overestimated by 6%, while the outer has the same magnitude as in Ashrafian [4].

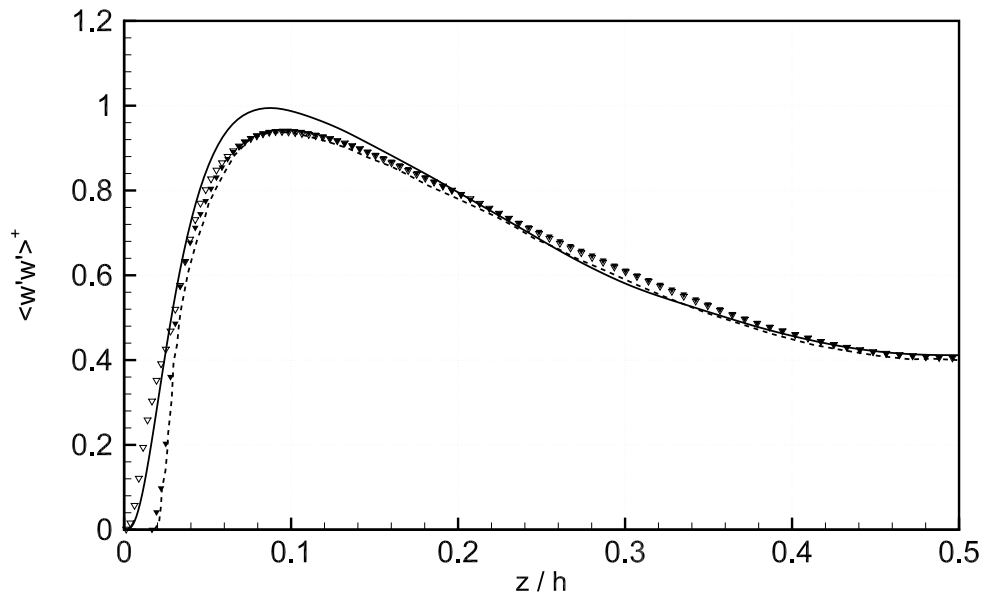


Figure 6.13: Wall-normal normal stress, $\overline{w'w'}^+$ in global coordinates. Mid crest (\blacktriangledown) and mid cavity (\triangledown) data. Line legend as in figure 6.11.

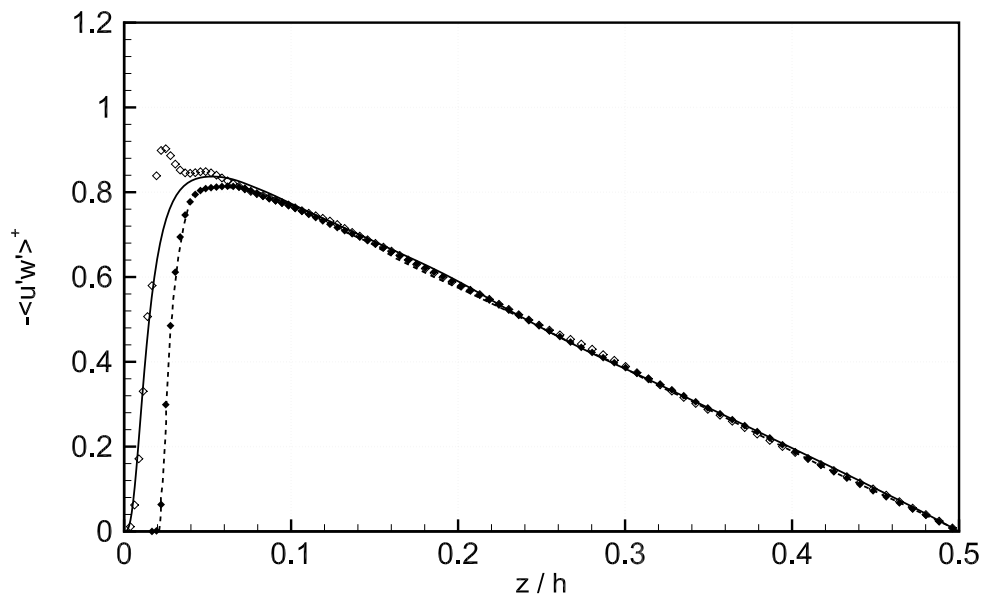


Figure 6.14: Reynolds shear stress, $-\overline{u'w'}^+$ in global coordinates. Mid crest (\blacklozenge) and mid cavity (\lozenge) data. Line legend as in figure 6.11.

6.4 Reynolds shear stress

The near wall behaviour of viscous and turbulent shear stress at the mid crest location is shown in 6.15. The viscous stress is $\tau_{viscous} = \nu du^+/dz$, normalized with u_τ , and the shear stress is, as before, $\tau_{turbulent} = -\overline{u'w'}^+$. The viscous part is in good agreement with the smooth channel data, as it is only dependent on the shape of $u^+(z)$. The shear stress data from Ashrafian [4] are perfectly collapsed with smooth channel data at $z^+ = 5r^+$, which is also the case for the turbulent shear stress in the present case. However, it must be said that the shear stress profile was not perfectly symmetric across the full channel height. The peak at the bottom and top half were in magnitude $\approx |0.74|$ and $\approx |0.88|$ respectively, making the average in good agreement with the smooth and rough channel data.

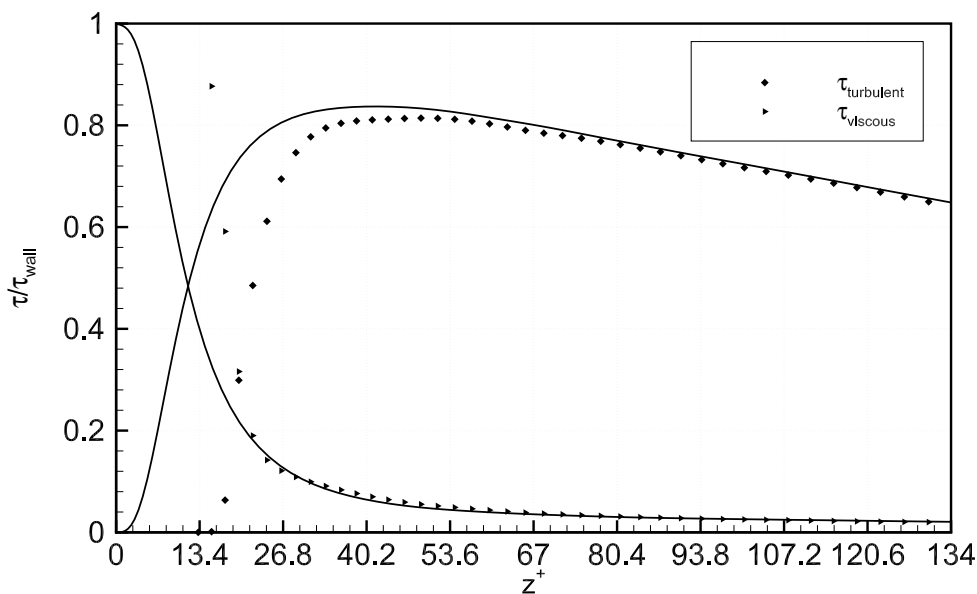


Figure 6.15: Near wall behaviour of shear stress at mid crest location. Solid lines are the smooth channel data of Moser et al. [41].

6.5 Turbulence kinetic energy

The turbulence kinetic energy is an important quantity in CFD, as most statistical closure models use a transport equation for the TKE to approximate the Reynolds stress term in equation (2.8) through the Boussinesq eddy viscosity assumption.

Figure 6.16 shows the instantaneous contour plot of the turbulence kinetic energy. The TKE is defined by equation (2.10), and in the figure, darker areas are associated with higher levels of TKE. Clearly, the region close to the roughness elements has much higher energy levels than the channel center. Also the cavity in between the elements has very low energy levels. The instantaneous plot also shows that the energy level around each roughness element in streamwise direction is rather

different. The averaged contour plot, however, shows smooth and streamwise periodic energy levels, according to what should be expected. This is perhaps with the exception of the first two ribs, where a higher peak can be observed at the top corner in the vicinity of the first rib, and a lower level for the second.

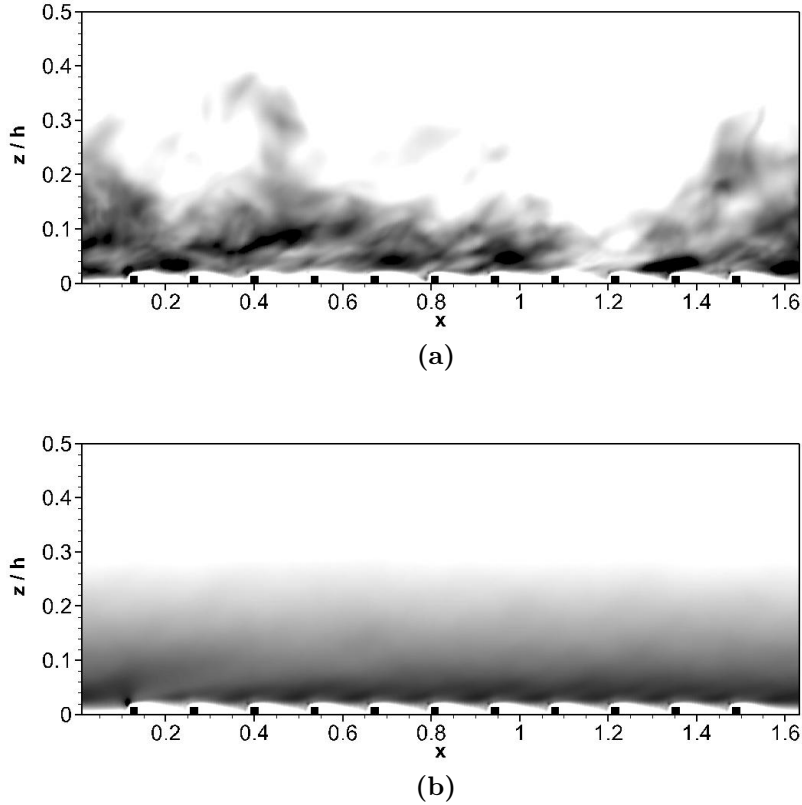


Figure 6.16: Instantaneous and averaged contour plot of turbulence kinetic energy.

Figure 6.17 shows the level of TKE at the mid crest and mid cavity locations, compared to the smooth channel data of Moser et al. [41]. The TKE peaks at almost the same level at both streamwise locations, but the position of maximum TKE for mid crest location is shifted one-half roughness height outwards. Outside $z^+ = 3r^+$, the profiles collapse for the two locations. The rough channel profiles converge smoothly to, and overlaps, the smooth channel data towards the channel center from $z^+ \approx 150$ (outside the range shown in figure 6.17), as was also indicated by the Reynolds normal stress plots.

Ashrafian [4] found that the point of maximum production and dissipation were $z^+ \approx 18$ and $z^+ \approx 13.6$, respectively, and that they are balanced ($P_k/\varepsilon \approx 1$) in the region $100 < z^+ < 200$. The peak in TKE was found to be $k \approx 3.3$ for both streamwise locations [5, fig.21], which is in good agreement with the present results.

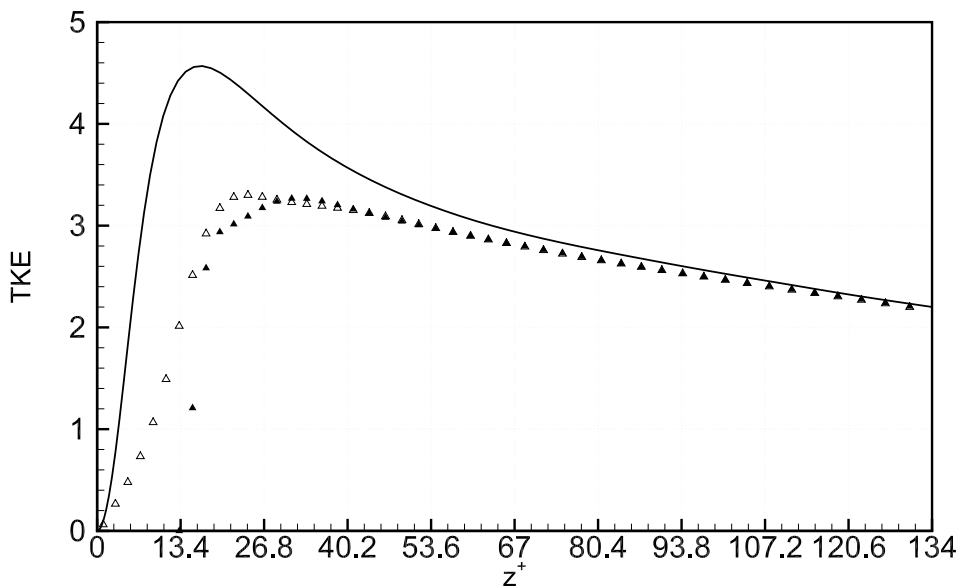


Figure 6.17: TKE in wall coordinates, normalized with u_τ . Mid crest (\blacktriangle) and mid cavity (\triangle) data. Solid line is smooth channel data from Moser et al. [41].

6.6 Vorticity

Figure 6.18 shows the r.m.s. of the vorticity fluctuations, where $\omega_{i,rms}^+$ is defined from equation (5.5). The vorticity statistics is of relevance, as it reflects the small scale structures of the flow. The figure can be compared to Ashrafian & Andersson [6, fig.2]¹³.

The streamwise component, $\omega_{x,rms}^+$, shows a minima at $z^+ = 5$ and a maxima at $z^+ = 15$, at the mid cavity location, which is in good agreement with both smooth channel data from Moser et al. [41], and data from Ashrafian & Andersson [6]. The magnitudes of the extrema is the same as in [6]. Mid crest, the profile has a distinct minima at $z^+ \approx 18$ in between two maxima, which is identical to [6]. But here, the values of the extrema differs about 5 – 15% compared to [6]. The spanwise $\omega_{y,rms}^+$ profiles collapses at $z^+ = 35$ with a magnitude of 0.14, which is identical to [6]. Mid cavity, the location and magnitude of the maxima is the same as [6], while the mid crest profile in [6] decreases more abrupt from the wall and out to $z^+ = 20$. Also, the extrema is overestimated by $\approx 40\%$ in the present simulation. The profiles for $\omega_{z,rms}^+$ shows the same trend as in [6] with the mid cavity and mid crest profiles collapsing around $z^+ \approx 30$, and location of the maxima at $z^+ = 18$ and $z^+ = 25$ respectively. The magnitudes of both maxima is, however, about 15% less.

¹³Or even better, Ashrafian [4, fig.2; article 2], but this figure is not included in the published article.

From $z^+ = 40$ and outwards, all profiles smoothly decrease to approximately the same magnitude. Further, at the mid cavity location, the difference between the components are smaller than in the smooth case, suggesting that the turbulence is more isotropic. Also, the profiles collapse with smooth channel data [41, fig.5] outside $z^+ \approx 50$, indicating that the vortical motions in the outer region are the same.

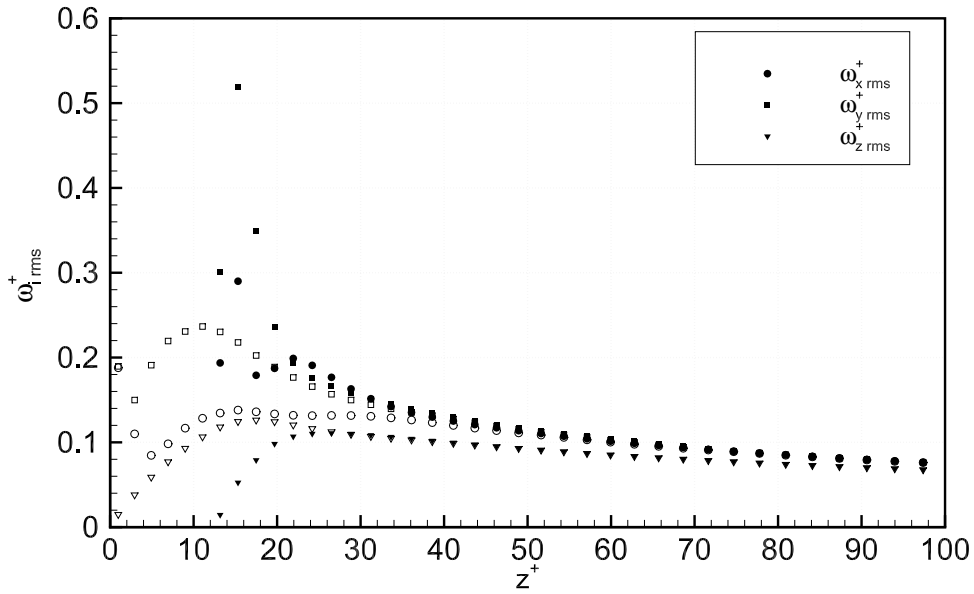


Figure 6.18: R.m.s. of vorticity fluctuations in wall coordinates. Filled symbols (\bullet , \blacksquare , \blacktriangledown) are mid crest data, while open symbols are mid cavity (\circ , \square , \triangledown) data.

7 Discussion

The smooth channel simulation is included in the thesis with the primary focus of getting familiar with DNS. Different aspects of these results will therefore not be thoroughly discussed, as the code has been used extensively by others for smooth channel simulations. Moreover, the primary focus from the rough wall simulation is not to discuss roughness effects, as this is more than well covered in the work of Ashrafian [4]. The following discussion serves more a supplement to the results and addresses some of the observed discrepancies, as well as numerical issues encountered during the work.

7.1 Statistics

At first, averaging was only performed in spanwise direction and in time. The first order statistics, i.e. mean velocity profiles, were smooth and in good agreement with available data from Ashrafian [4], but the profiles of second order statistics were not perfectly smooth, despite showing the same trends. To obtain better statistics, unit-wise averaging was performed, resulting in much smoother profiles. Further, figure 6.3 and 6.8 show that the solution is not fully symmetric about the channel centreline. Averaging was therefore performed over both sides, finally resulting in statistics being in agreement with the available data from literature. In the rough channel reference case [4], the same averaging is performed, both unit-wise and over the channel height. Due to a longer streamwise domain length, unit-wise averaging could, however, be performed over 24 samples, 13 more than the present case.

Moreover, the post processing code had to be modified to remove mean spanwise and wall-normal velocities in the calculation of fluctuations in these respective directions, as the plane channel code did not account for mean velocities in any other directions than in the streamwise direction.

7.2 Domain size

The results from the smooth channel simulation indicates that domain size influence is significant, as the grid point resolution was sufficient, being approximately

the same as used by Kim et al. [32]. Even though mean velocity profiles are quite accurate, the second order statistics reveals noticeable deviations from the data of Kim et al. [32]. The results from the rough channel is also believed to be influenced by the domain size, as it is shown by Ashrafian [4] that the lengths of the computational domain used in his study was necessary.

To ensure the adequacy of the domain size, two-point correlation coefficients can be calculated. In effect, this is a measure of how the flow at one point in the domain affects the flow in another point of the domain. In a domain of sufficient size, the coefficients should decrease to zero. Kim et al. [32] also use two-point correlations to prove that the domain size is sufficient. Ashrafian [4] started from $(L_x, L_y) = (3/4\pi, 3/4\pi)$, but the correlation factors were not sufficiently small until the lengths $(L_x, L_y) = (2\pi, \pi)$ were chosen, which essentially corresponds to the size of the smooth channel of Moser et al. [41]. This was despite the fact that roughness was believed to shorten the coherence, which would allowed for a smaller domain to be used. Further, the periodic boundary conditions used implies, effectively, that the box is infinite in size. In other words, that it has no surface.

7.3 Grid resolution

The grid point resolution is important, as it determines which scales are represented. In a direct simulation, all scales must be resolved, including the smallest scales, which are important regarding the dissipation of turbulence energy, i.e. the Reynolds normal stresses.

Moin & Mahesh [40, p.544] states that actually using a grid size equal to, or less than the Kolmogorov scale is too stringent. It needs to be of the order $O(\eta)$, as spectral DNS has proved to be accurate, even though the Kolmogorov scale is not fully resolved. Kim et al. [32, p.135] also used a spectral-method, and notes that the grid spacing used was 2 wall units larger than the estimated Kolmogorov length scale. Using modified wavenumber error analysis, it can be shown that for a specific wavelength of 3η to be represented with at least 5% accuracy, a central second order finite difference scheme needs a grid spacing of 0.26η , while a Fourier representation needs 1.5η [40, p.545]. Also, a previously mentioned rule of thumb is that a spectral method with N collocation points is more accurate than a finite difference scheme using $2N$ points [21, p.85]. Clearly, the level of accuracy, resulting from the exact computation of derivatives in Fourier space, is different. Having this in mind, when accounting for reduced domain size, the grid resolution is 43% less than in the case of Ashrafian [4], all of which are in the spanwise and streamwise directions, where the more accurate spectral-method is used. As indicated by the results, about the same level of accuracy seems to be delivered.

Regarding the resolution of the roughness elements, 6 and 3 grid points resolves the roughness in wall-normal and streamwise directions respectively, compared to 8 and 4 in [4]. Also, out to a distance of $z^+ = 3r^+$ inside the roughness sublayer, Ashrafian [4] use 24 points compared to 18 in the present study. More intensive grid stretching or a finer grid with constant height in the roughness sublayer could have

been used. For the streamwise direction, grid stretching, such as used by Ikeda & Durbin [28], cannot be implemented in the present study, but this was not used by Ashrafian [4] either.

Further, using the spectral-method revealed that the number of grid points had to be wisely chosen to be able to run the code. With $N_x = 144$ or $N_x = 240$ for example, the code did not work. In streamwise direction, number of points also had to coincide with the given roughness size and spacing, putting some restrictions on the choice of grid resolution and domain length. As Pope [46, p.345] states, N is often chosen to be in powers of 2. $N_x = 288$ was used, and the domain length was adjusted accordingly to coincide with the roughness.

For the rough channel, noticeable deviation from the results of Ashrafian [4] is only found in some of the vorticity statistics (r.m.s. of vorticity fluctuations), in addition to the existence of a mean spanwise velocity, v^+ . This is likely to be related, first of all, to the poor spanwise grid resolution, then to the inadequate spanwise length, L_y . Having more statistical samples in time could possibly also have improved this. The presented results in this thesis are also quite limited compared to what is possible to extract from a DNS-simulation. Larger deviations in higher order statistics, compared to the data of Ashrafian [4], may exist, but this remains unknown.

7.4 Roughness elements

The roughness elements is implemented as described in section 4.4.4, by setting the three velocity components to zero inside the roughness. For the boundaries, the streamwise grid point locations coincides with the prescribed roughness size, which is the same method as used by Narasimhamurthy & Andersson [42]. This is easy to implement, and implies that more advanced immersed body methods, such as used in the studies of Ikeda & Durbin [28] and Leonardi et al. [39], does not have to be used.

For the wall normal direction however, the calculation of wall-normal grid point locations is the same as used in the original code, equation (4.18). Thus, caution regarding both the prescribed roughness height and cell growth ratio had to be taken, as aggressive grid stretching may lead to numerical instabilities. A stretch factor of $s = 3$ in equation (4.18) was found to be suitable, as the grid stretching is quite moderate, and at the same time caused the grid points to coincide best with the wanted height of the roughness. As a consequence of doing so, the roughness height is not perfectly $r = 0.017h$, but rather $r = 0.0167h$, which in wall coordinates corresponds to $r^+ = 13.2$.

Further, the staggered wall-normal configuration causes the top boundary specification in the code to be non-physical, as the wall normal velocity is set to zero at the cell face, which is essentially outside the roughness surface. However, this was not found to affect the results in the vicinity of the surface. The grid has a high resolution at this location, so the effect will be limited anyway. Inspection of the velocity data files in Tecplot, where cell-face variables are interpolated to

cell-centres, confirmed that all velocity components were zero inside, and exactly on the surfaces of the roughness.

Despite having these known flaws, using the code as it is described here was motivated by ease of implementation, and the fact that it did not seem to affect the solution at all. In retrospective view, however, wall-normal grid point locations should have been chosen to coincide perfectly with the roughness height, by replacing or modifying equation (4.18) to better suit this specific application.

7.5 Inhomogeneity

As Pope [46, p.353] states, there are some principal differences when applying DNS to inhomogeneous flows. Some are that Fourier representations cannot be used, physical boundaries are required, and additional grid resolution requirements arises near walls. Clearly, for the very inhomogeneous wall-normal direction all of this applies, and a finite difference scheme is used. For the present case, the inhomogeneous streamwise direction is not related to walls, and moreover, using periodic boundary conditions is justified, or preferred even. The streamwise direction is by definition inhomogeneous, but still, a quasi-homogeneity exists, as the flow pattern is repetitive. Also, the inhomogeneous flow pattern is very restricted to the roughness sublayer, stretching out to approximately $z^+ = 5r^+ = 67$. Considering both sides, this is 17% of the channel height. The results may indicate that this periodicity, or quasi-homogeneity is sufficient, as the variables, represented by complex Fourier-series, will still have some degree of periodicity. For comparison, all comparable DNS-studies of surface roughness, e.g. [39, 28, 7, 42], use staggered finite-difference schemes in all directions.

Also, a simulation was run using rectangular ribs having a height four times the width. The bulk velocity rapidly decreased below 8, but the simulation was not run long enough for a statistically steady state to be obtained. The already low bulk velocity may indicate the need for a higher Reynolds number, in effect a higher pressure gradient, for the turbulence to be sustained. There was, however, not enough time for proper investigation of this simulation, but at least the code run without numerical issues, even though the level of inhomogeneity in streamwise direction increased significantly compared to the small roughness elements used originally.

7.6 Further work

As it is shown that the code works when a small streamwise inhomogeneity is introduced, larger roughness elements should be implemented. The simulations of Leonardi et al. [39] and Narasimhamurthy & Andersson [42] use considerable larger ribs, $r = 0.2\delta$ and $r = 0.1\delta$ respectively, and can be used for comparison. Further, it would be interesting to see whether the presence of uneven roughness elements affects code performance. A variable height-to-pitch ratio or uneven height of the

elements can be imposed to remove some of the streamwise quasi-homogeneity. Ikeda & Durbin [28] performed simulations where roughness height was increased and decreased by 15% compared to the original height.

Details concerning grid resolution and domain size should also be addressed. It is evident that this influences the results, thus the dependency should be investigated. Further studies can definitely benefit from more grid points in spanwise direction, as well an implementation of a better suited grid stretching in wall-normal direction. More effort can also be paid regarding the roughness top surface boundary condition for the staggered wall-normal velocity. The Kolmogorov micro scale can also be computed from the dissipation rate, and then be compared to the grid resolution used. Further, correlation coefficients can be calculated to check the adequacy of the streamwise and spanwise domain lengths.

Regarding the post processing, the budgets, e.g. for the TKE and second moment equations, as well as higher order moments can be obtained.

8 Conclusion

Direct Numerical Simulations of pressure driven channel flow has been performed for a smooth channel at Reynolds number $Re_\tau = 180$ and rough channel at Reynolds number $Re_\tau = 395$.

Despite having sufficient grid resolution, effectively the same as the reference case of Kim et al. [32], the smooth channel simulation indicates that there is a substantial effect of reduced domain size, especially for the second order statistics.

The presented results from the rough channel flow is almost identical to what is found by Ashrafian [4]. With the exception of the vorticity statistics, maximum deviations is found to be about 5%. The results supports the wall similarity hypothesis, which implies there is no streamwise dependency in the outer layer, i.e. that the flow is unaware of the surface conditions outside the roughness sublayer. The shift in mean velocity profile is found to be $\Delta u^+ = 7.1$, and in terms of streamwise dependency, u^+ is affected out to $z^+ \approx 60$. The root mean square of the velocity fluctuations and the Reynolds normal stresses is found to be influenced by roughness out to $z \approx 5r^+$, while streamwise dependency is found to exist out to $z^+ \approx 3r^+$, as the mid crest and mid cavity profiles collapses at this location.

The results obtained from the pseudo-spectral code, using a grid resolution reduced by 43% compared to Ashrafian [4], indicates that a high level of accuracy is still delivered. The reduction of domain size and grid points is of course motivated by reduced computational cost, but also to check the spectral method's superior accuracy and reduced demand for grid resolution. The results, however, are still believed to be influenced by two different effects, the very poor spanwise grid resolution and the size of the computational domain, as indicated by the presence of a mean spanwise velocity.

It is proven that the pseudo-spectral DNS-code works well using roughness elements of the height $r = 0.017h$, with a spacing of $7r$. The spectral method's Fourier-basis demands that the variables being represented are periodic, and the results suggests that the quasi-homogeneity of the velocity field is sufficient for the code to deliver accurate results. However, only a small part of the flow field, effectively in the roughness sublayer, is quasi-homogeneous, while the core flow is more or less unaffected, still being homogeneous.

References

- [1] Adams, N. A., Stolz, S., Schlatter, P., Ziefle, J., Härtel, C., and Kleiser, L. (2012). *Grundlagen der Numerischen Strömungsmechanik*. Lehrstuhl für Aerodynamik und Strömungsmechanik, Technische Universität München.
- [2] Anderson Jr., J. D. (2011). *Fundamentals of Aerodynamics, 5.th Edition*. McGraw-Hill Education.
- [3] Antonia, R. A. and Krogstad, P.-Å. (2001). Turbulence Structure in Boundary Layers Over Different Types of Surface Roughness. *Fluid Dynamics Research*, 28(2):139–157.
- [4] Ashrafian, A. (2004). *Numerical Investigation of Turbulent Flow in a Channel With Rough Walls*. PhD thesis, Norwegian University of Science and Technology, Departement of Energy and Process Engineering.
- [5] Ashrafian, A. and Andersson, H. I. (2006a). Roughness Effects in Turbulent Channel Flow. *Progress in Computational Fluid Dynamics, an International Journal*, 6(1):1–20.
- [6] Ashrafian, A. and Andersson, H. I. (2006b). The Structure of Turbulence in a Rod-Roughened Channel. *International Journal of heat and Fluid Flow*, 27(1):65–79.
- [7] Ashrafian, A., Andersson, H. I., and Manhart, M. (2004). DNS of Turbulent Flow in a Rod-Roughened Channel. *International Journal of Heat and Fluid Flow*, 25(3):373–383.
- [8] Bakken, O. M. (2004). *Experimental Investigation of Turbulent Flow in a Channel With Rough Walls*. PhD thesis, Norwegian University of Science and Technology, Departement of Energy and Process Engineering.
- [9] Bandyopadhyay, P. R. (1987). Rough-Wall Turbulent Boundary Layers in the Transition Regime. *Journal of Fluid Mechanics*, 180:231–266.
- [10] Bhaganagar, K., Kim, J., and Coleman, G. (2004). Effect of Roughness on Wall-Bounded Turbulence. *Flow, Turbulence and Combustion*, 72(2-4):463–492.

-
- [11] Boersma, B. J. (2000). FORTRAN program files; Pseudo-Spectral DNS-code.
- [12] Canuto, C., Hussaini, M. Y., Quarteroni, A., and Zang, T. A. (2006). *Spectral Methods, Fundamentals in Single Domains*. Springer.
- [13] Canuto, C., Hussaini, M. Y., Quarteroni, A., and Zang, T. A. (2007). *Spectral Methods, Evolution to Complex Geometries and Applications to Fluid Dynamics*. Springer.
- [14] Chorin, A. J. (1968). Numerical Solution of the Navier-Stokes Equations. *Mathematics of Computation*, 22(104):745–762.
- [15] Clauser, F. H. (1956). The turbulent Boundary Layer. *Advances in Applied Mechanics*, 4:1–51.
- [16] Cui, J., Patel, V. C., and Lin, C. L. (2003). Large-Eddy Simulation of Turbulent Flow in a Channel With Rib Roughness. *International Journal of Heat and Fluid Flow*, 24(3):372–388.
- [17] Davidson, L. (2011). An Introduction to Turbulence Models. Technical report, Department of Thermo and Fluid Dynamics, Chalmers University of Technology.
- [18] Davidson, L. (2013). Fluid Mechanics, Turbulent Flow and Turbulence Modeling. Technical report, Division of Fluid Dynamics, Department of Applied Mechanics, Chalmers University of Technology.
- [19] Durbin, P. A. and Petterson-Reif, B. A. (2011). *Statistical Theory and Modeling for Turbulent Flows*. John Wiley & Sons.
- [20] Ertesvåg, I. S. (2000). *Turbulent Strøyming og Forbrenning; Frå turbulensteori til Ingeniørverkty*. Tapir Akademiske Forlag.
- [21] Ferziger, J. H. (1998). Direct and Large Eddy Simulation of Turbulence. *Centre de Recherches Mathematiques CRM, Proceedings and Lecture Notes*, 16:53–97.
- [22] Ferziger, J. H. and Peric, M. (2002). *Computational Methods for Fluid Dynamics, 3rd Edition*. Springer.
- [23] Furuya, Y., Miyata, M., and Fujita, H. (1976). Turbulent Boundary Layer and Flow Resistance on Plates Roughened by Wires. *Journal of Fluids Engineering*, 98(4):635–643.
- [24] Gillissen, J. (2008). *Numerical Simulation of Fibre-Induced Drag Reduction in Turbulent Channel Flow*. PhD thesis, Laboratory for Aero- and Hydro Dynamics at the Delft University of Technology, Netherlands.
- [25] Gillissen, J. J. J., Boersma, B., Mortensen, P. H., and Andersson, H. I. (2008). Fibre-Induced Drag Reduction. *Journal of Fluid Mechanics*, 602:209–218.

-
- [26] Gillissen, J. J. J., Boersma, B. J., Mortensen, P. H., and Andersson, H. I. (2007). On the Performance of the Moment Approximation for the Numerical Computation of Fiber Stress in Turbulent Channel Flow. *Physics of Fluids (1994-present)*, 19(3):035102.
- [27] Hanjalic, K. and Launder, B. E. (1972). Fully Developed Asymmetric Flow in a Plane Channel. *Journal of Fluid Mechanics*, 51(02):301–335.
- [28] Ikeda, T. and Durbin, P. A. (2007). Direct Simulations of a Rough-Wall Channel Flow. *Journal of Fluid Mechanics*, 571:235–263.
- [29] Jiménez, J. (2004). Turbulent Flows Over Rough Walls. *Annu. Rev. Fluid Mech.*, 36:173–196.
- [30] Jiménez, J. and Pinelli, A. (1999). The Autonomous Cycle of Near-Wall Turbulence. *Journal of Fluid Mechanics*, 389:335–359.
- [31] Kim, J. and Moin, P. (1985). Application of a Fractional-Step Method to Incompressible Navier-Stokes Equations. *Journal of Computational Physics*, 59(2):308–323.
- [32] Kim, J., Moin, P., and Moser, R. D. (1987). Turbulence Statistics in Fully Developed Channel Flow at Low Reynolds number. *Journal of Fluid Mechanics*, 177:133–166.
- [33] Kreyszig, E. (2006). *Advanced Engineering Mathematics, 9.th Edition*. John Wiley & Sons.
- [34] Krogstad, P.-Å., Andersson, H. I., Bakken, O. M., and Ashrafian, A. (2005). An Experimental and Numerical Study of Channel Flow with Rough Walls. *Journal of Fluid Mechanics*, 530:327–352.
- [35] Krogstad, P.-Å. and Antonia, R. A. (1999). Surface Roughness Effects in Turbulent Boundary Layers. *Experiments in Fluids*, 27(5):450–460.
- [36] Krogstad, P.-Å., Antonia, R. A., and Browne, L. W. B. (1992). Comparison Between Rough-and Smooth-Wall Turbulent Boundary Layers. *Journal of Fluid Mechanics*, 245:599–617.
- [37] Launder, B. E. (1993). An Introduction to Single-Point Closure Methodology. *VKI An Introduction to Modeling Turbulence*, 1.
- [38] Leonardi, S., Orlandi, P., Djenidi, L., and Antonia, R. A. (2004). Structure of Turbulent Channel Flow with Square Bars on One Wall. *International Journal of Heat and Fluid Flow*, 25(3):384–392.
- [39] Leonardi, S., Orlandi, P., Smalley, R. J., Djenidi, L., and Antonia, R. A. (2003). Direct Numerical Simulations of Turbulent Channel Flow with Transverse Square Bars on One Wall. *Journal of Fluid Mechanics*, 491:229–238.

-
- [40] Moin, P. and Mahesh, K. (1998). Direct Numerical Simulation: A Tool in Turbulence Research. *Annual Review of Fluid Mechanics*, 30(1):539–578.
- [41] Moser, R. D., Kim, J., and Mansour, N. N. (1999). Direct Numerical Simulation of Turbulent Channel Flow Up to $Re = 590$. *Physics of Fluids*, 11(4):943–945.
- [42] Narasimhamurthy, V. D. and Andersson, H. I. (2014). Turbulence Statistics in a Rotating Ribbed Channel. *International Journal of Heat and Fluid Flow*.
- [43] Nikuradse, J. (1933). Strömungsgestze in Rauhen Röhren. *VDI-Forschungsheft 361, English transl., NACA Technical Memorandum 1292*.
- [44] Perry, A. E. and Abell, C. J. (1977). Asymptotic Similarity of Turbulence Structures in Smooth-and Rough-Walled Pipes. *Journal of Fluid Mechanics*, 79(04):785–799.
- [45] Perry, A. E., Lim, K. L., and Henbest, S. M. (1987). An Experimental Study of the Turbulence Structure in Smooth-and Rough-Wall Boundary Layers. *Journal of Fluid Mechanics*, 177:437–466.
- [46] Pope, S. B. (2000). *Turbulent Flows*. Cambridge University Press.
- [47] Raupach, M. R., Antonia, R. A., and Rajagopalan, S. (1991). Rough-Wall Turbulent Boundary Layers. *Applied Mechanics Reviews*, 44(1):1–25.
- [48] Schlichting, H. (1968). *Boundary-Layer Theory*. McGraw-Hill.
- [49] Schlichting, H. and Gersten, K. (2000). *Boundary-Layer Theory, 8.th Revised and Enlarged Edition*. Springer.
- [50] Temam, R. (1969). Sur l’approximation de la solution des équations de Navier-Stokes par la méthode des pas fractionnaires (II). *Archive for Rational Mechanics and Analysis*, 33(5):377–385.
- [51] Tennekes, H. and Lumley, J. L. (1972). *A First Course in Turbulence*. MIT press.
- [52] Townsend, A. A. (1976). *The Structure of Turbulent Shear Flow*. Cambridge University Press.
- [53] Vreman, A. W. (2014). The Projection Method for the Incompressible Navier–Stokes Equations: The Pressure Near a No-Slip Wall. *Journal of Computational Physics*, 263:353–374.
- [54] White, F. M. (2006). *Viscous Fluid Flow, 3rd Edition*. The McGraw-Hill Companies New York.
- [55] White, F. M. (2008). *Fluid Mechanics, 6.th Edition*. The McGraw-Hill Companies New York.
- [56] Zhao, L. (2012). *Particles in Wall Turbulence*. PhD thesis, Norwegian University of Science and Technology, Departement of Energy and Process Engineering.